Lithos 360–361 (2020) 105441

Contents lists available at ScienceDirect

Lithos

journal homepage: www.elsevier.com/locate/lithos

Research Article

New constraints on the onset age of the Emeishan LIP volcanism and implications for the Guadalupian mass extinction

Hao Yan [a,b], Dao-Hui Pi [a,*], Shao-Yong Jiang [a,*], Weiduo Hao [b], Kaarel Mänd [b,d], Leslie J. Robbins [c], Long Li [b], Kurt O. Konhauser [b]

[a] State Key Laboratory of Geological Processes and Mineral Resources, School of Earth Resources, China University of Geosciences, Wuhan, China
[b] Department of Earth & Atmospheric Sciences, University of Alberta, Edmonton, AB, Canada
[c] Department of Geology & Geophysics, Yale University, New Haven, CT, USA
[d] Department of Geology, University of Tartu, Tartu, Estonia

ARTICLE INFO

Article history:
Received 27 October 2019
Received in revised form 19 February 2020
Accepted 20 February 2020
Available online 24 February 2020

Keywords:
Emeishan large Igneous Province
Onset age
Guadalupian mass extinction
Maokou Formation
South China

ABSTRACT

The onset of the Middle Permian Emeishan Large Igneous Province (ELIP), is commonly implicated in the Guadalupian mass extinction, one of the largest Phanerozoic extinction events, yet the contribution of the ELIP to this biotic event remains unresolved because of a lack of appropriate age constraints. In this study, we examined claystone beds overlying the cherty limestone of the Maokou Formation and underlying the flood basalts of the ELIP that were emplaced around the Guadalupian-Lopingian Boundary. Integrated petrographic, mineralogical, elemental, and isotopic features indicate that the studied claystones contain significant components from mafic volcanic ash that was likely associated with the emplacement of the ELIP. Zircons from the claystones yield U—Pb ages of ~262.5 Ma, which predates the subaerial eruptive phase of the ELIP (259.1–260.4 Ma), but is comparable to the *J. altudaensis* conodont biostratigraphic zone (~263 Ma, Middle Capitanian Stage) which is contemporaneous with the emplacement of early-stage Emeishan subaqueous pillow basalts and mafic volcaniclastics. Our data provide a crucial new constraint on the lower age limit for the onset of the ELIP, which was likely associated with violent submarine eruptions and thus could have contributed to the loss of marine fauna during the Guadalupian mass extinction.

1. Introduction

The Middle to Late Permian transition was marked by one of the major biological crises of the Phanerozoic, known as the Guadalupian mass extinction (Bond et al., 2019; Grasby et al., 2016; Wignall et al., 2009a; Yang et al., 2004). The most notable losses during the Guadalupian mass extinction were amongst the fusulinid foraminifers (Wignall et al., 2009b; Yang et al., 2004), and occurred at the beginning of the *J. xuanhanensis* conodont zone (Lai et al., 2008; Wignall et al., 2009a), corresponding to an absolute age of around 262.0 Ma for the mass extinction pulse (Ogg et al., 2016), which predates the Guadalupian-Lopingian Boundary (G-LB) (259.8 ± 0.4 Ma, Henderson et al., 2012).

Although the ultimate cause of the Guadalupian extinction in South China remains debated, the eruptive phase of the Emeishan Large Igneous Province (ELIP) around the G-LB has been suggested by a number of studies to be the underlying cause (Bond et al., 2010a, 2010b; Saitoh et al., 2013; Shellnutt, 2014; Zhou et al., 2002). Studies over the past two decades have suggested that a highly explosive and voluminous silicic volcanic eruptive phase (as recorded by the volcanic rocks) postdates the flood basalt eruptive phase of the ELIP (Xu et al., 2010; Yang et al., 2015; Zhao et al., 2016) and may be correlative with the Guadalupian mass extinction. However, zircon ages from these silicic volcanic rock layers are ~259.1 ± 0.5 Ma (Huang et al., 2016; Zhong et al., 2014), which is younger than the biostratigraphic constraints that place the mass extinction at ~262 Ma (Wignall et al., 2009a, 2009b). Instead, an $^{40}Ar/^{39}Ar$ age of 260.1 ± 1.2 Ma for the earlier flood basalt phase of the Emeishan volcanism, suggests a link between the basaltic eruptions and the Guadalupian mass extinction (Li et al., 2018). Yet, despite a matching age, these flood basalts are considered to an unlikely instigator of the biotic crisis, since they are dominantly effusive and thus unlikely to have resulted in major stratospheric sulphur loading and a regional atmospheric impact (Ross et al., 2005; Yang et al., 2015).

Based on the identification of subaerial silicic and flood basaltic lava flows, more recent studies have argued that the emplacement of voluminous subaqueous pillow basalts with mafic submarine hyaloclastite deposits during an early eruption stage of the ELIP may represent a mechanism sufficient to impact the Guadalupian environment (Jerram

* Corresponding authors.
E-mail addresses: daohuipi@cug.edu.cn (D.-H. Pi), shyjiang@cug.edu.cn (S.-Y. Jiang).

https://doi.org/10.1016/j.lithos.2020.105441
0024-4937/

et al., 2016; Ukstins Peate and Bryan, 2008; Wignall et al., 2009b; Zhu et al., 2014, 2019). Although the age of these pillow basalts and associated mafic volcaniclastics can be constrained through conodont biostratigraphy to be in the *J. altudaensis* zone of the Capitanian Stage (~263 Ma, Ogg et al., 2016), which predates the loss of the fusulinid foraminifers at 261 Ma (Lai et al., 2008; Sun et al., 2010;

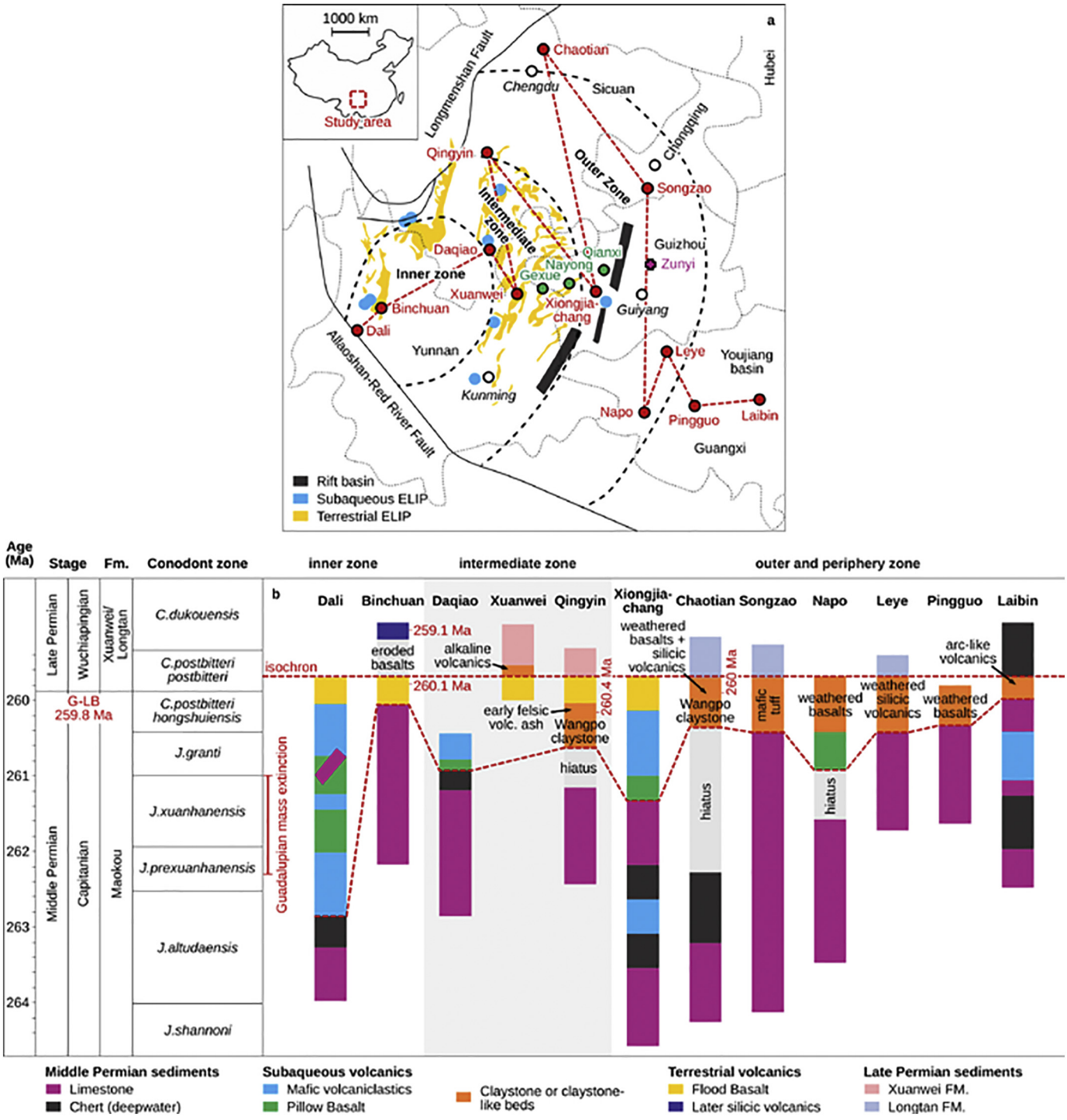

Fig. 1. (a) Distribution of sedimentary sections on the Guadalupian-Lopingian boundary (G-LB) in the Emeishan Large Igneous Province (ELIP) (modified from He et al., 2003). The black dashed lines indicate the boundaries of the three Emeishan Large Igneous Province (ELIP) zones, arranged in a concentric manner into inner, intermediate, and outer zones around the hypothesized core of the surficial uplift. Bold names: ELIP zones; normal text: province names; italics and black circles: the respective provincial capitals; red circles and names: relevant sections taken from the literature and discussed in the paper. Green and purple symbols and names indicate the studied manganese deposits and claystone beds reported by Gao et al. (2018). (b) Comparison of the sedimentary record across the G-LB from the ELIP center to its periphery (beyond ~100 km), corresponding to the red circles and line in (a). Standard international conodont biozones (Ogg et al., 2016) and recognized chrono- and lithostratigraphic units, as well as major geological events around the G-LB are shown on the left. Notable features include the Guadalupian mass extinction (Lai et al., 2008; Wignall et al., 2009a) and the widespread development of deep-water, cherty limestone facies in the *J. altudaensis* zone shortly before the first phase of volcanism, indicating pre-volcanic platform collapse (deepening). References for the Dali section: Jerrram et al. (2016) and Zhu et al. (2014, 2019); Binchuan: He et al. (2007) and Li et al. (2018); Daqiao: Ukstins Peate et al. (2008); Xuanwei: He et al. (2007) and Zhao et al. (2016); Qingyin: Huang et al. (2016); Xiongjiachang: Sun et al. (2010); Chaotian: He et al. (2007); Songzao: Dai et al. (2011); Napo: Huang et al. (2014); Leye: Yu et al. (2016); Pingguo: Liu et al. (2017); Laibin: Wignall et al. (2009b) and Zhong et al. (2013).

Wignall et al., 2009a, 2009b), the paucity of zircon U—Pb ages for these volcaniclastics represents a significant obstacle to linking the early eruptive phase to the extinction phase at the end of the Guadalupian.

Besides the pillow basalts and mafic volcaniclastics, abundant ELIP volcanism-related claystone beds also occur around the G-LB in southwest China (Isozaki et al., 2004; Saitoh et al., 2013; Sun et al., 2010; Zhang et al., 2007). Given the possible derivation of these claystones from and emplacement during the early ELIP volcanism, they have been invoked as a way to link the timing of the volcanism to the mass extinction (He et al., 2010; Zhong et al., 2014). However, their source remains disputed and their ages poorly resolved. For example, the claystone in the Wangpo Bed (Fig. 1), which overlies the Middle Permian Maokou Formation limestones and underlies the Emeishan flood basalts (or, where basalts are absent, the limestones of the Late Permian Wuchiaping Formation; He et al., 2007; Huang et al., 2016; Sun et al., 2008, 2010) is considered to be derived from the volcanic ash of an early pulse of Emeishan felsic volcanism (Huang et al., 2016; Isozaki et al., 2004). Accordingly, a zircon age (~260.4 ± 1.2 Ma) from the Wangpo Bed was interpreted as representing the initial eruption of the main flood basaltic phase (Huang et al., 2016) and has been taken as a comparable age with the mass extinction. The weathering of flood basalts and later silicic volcanics has also been proposed as an alternative origin of the Wangpo Bed (Deconinck et al., 2014; He et al., 2007, 2010; Shao et al., 2017). In contrast, studies on stratigraphically equivalent claystone beds in the Songzao region suggest that these claystones originated from mafic tuff (Dai et al., 2010, 2011; Zou et al., 2016). Integrated origin and age information of these claystone beds is critical to understanding which type of volcanism in the ELIP was responsible for the Guadalupian mass extinction.

In this work we present whole-rock geochemistry, Sr-Nd-Pb isotopes, zircon U—Pb dates, and Lu—Hf isotopic data from the claystone layers located at the foot and hanging wall of the Middle to Late Permian deep-water Zunyi manganese (Mn) deposit that underlies the ELIP flood basalts (Gao et al., 2018). Geochemical evidence presented here suggest that the source of the claystones were mafic tuffs from the early stage of ELIP volcanism, constrained to ~262.5 Ma. These data support the influence of early submarine mafic ELIP volcanism on the Guadalupian mass extinction.

2. Geological background

2.1. Late Permian sedimentary systems in South China and the Emeishan large igneous province

The ELIP is comprised of voluminous subaqueous pillow basalts with mafic submarine hyaloclastite (tuff) deposits that formed during the early stages of eruption, and subsequent terrestrial flood basalts, picrites, mafic/ultramafic intrusions, and felsic rocks (trachytes and rhyolites) that characterize the later eruptive phases (Ali et al., 2005; Huang et al., 2014; Shellnutt, 2014; Xiao et al., 2004; Xu et al., 2010; Zhang et al., 2006; Zhou et al., 2006; Zhu et al., 2014, 2019). The main terrestrial phase of the ELIP volcanism has been dated to near the G—LB at 259.8 ± 0.4 Ma with an estimated duration of ~1 Ma (Henderson et al., 2012; Huang et al., 2016; Metcalfe et al., 2015; Shellnutt et al., 2012; Zhong et al., 2014). The ELIP volcanism influenced an area of ~250,000 km^2, extending from the inner zone in Yunnan province, through the Guizhou, Sichuan and Chongqing provinces, to its periphery in the Youjiang Basin in Guangxi province (Fig. 1a; Ali et al., 2005).

During the Early to Middle Permian, a carbonate platform covered the South China Block (ESC, 2000). During the Middle to Late Guadalupian, this carbonate platform evolved into three distinct sedimentary zones as a result of the Emeishan volcanism (Fig. 1a; He et al., 2003). In the inner zone (e.g., in the Binchaun region; Fig. 1b), the Emeishan flood basalts and rare later silicic volcanic rocks cover the Middle Permian limestone of the Maokou Formation (He et al., 2007; Xu et al., 2010; Zhu et al., 2014, 2019). In some areas (e.g., in the Dali region; Fig. 1b), there exist abundant pillow basalts with mafic submarine volcaniclastics between the Middle Permian Maokou sequence and the Emeishan flood volcanic rocks. In the intermediate zone, claystone beds associated with the Emeishan mafic submarine volcaniclastics or flood basalts unconformably overlie the Maokou Formation, but conformably underlie the Xuanwei Formation. The latter is a terrestrial late Permian unit with a thickness of ~100–300 m in the eastern Yunnan and western Guizhou provinces (e. g., in the Daqiao, Qingyin, and Xuanwei regions; Fig. 1b). In the outer zone, particularly on the periphery of the ELIP volcanism, a continuous carbonate platform was developed with fewer Emeishan volcanic rocks during the Permian. A marine regression at the G-LB resulted in the deposition of a variably thick claystone between the Longtan and Maokou formations (e.g., in the Chaotian and Songzao regions; Fig. 1b). This particular sedimentary sequence extends to the Napo, Pingguo and Leye regions in the Youjiang Basin in Guangxi province as claystone-like beds (mudstones and bauxite) (Fig. 1b). In the Xiongjiachang and Laibin regions (Fig. 1b), there are also mafic submarine volcaniclastics interbedded with cherts in the Maokou Formation. Of note is the widespread development of deep-water, cherty limestone facies in the *J. altudaensis* zone shortly before the first phase of volcanism, indicating pre-volcanic platform collapse and corresponding basin deepening (Lai et al., 2008; Sun et al., 2010; Zhu et al., 2019).

2.2. Deposit description

Before the eruption of the early-stage subaqueous ELIP there was a drowning event with deep-water facies (cherts) developing in the *J. altudaensis* zone as a consequence of the subsidence of the restricted shallow water carbonate platform (Jerram et al., 2016; Sun et al., 2010; Zhu et al., 2014, 2019). A series of deepwater platform gullies extend along a northeast to southwest direction from Zunyi, Nayong, and Shuicheng (Guizhou Province) to Geyun (Yunnan Province) and are preserved in the outer and intermediate zones of the ELIP (Fig. 2a). These gullies could have been ~25–35 km in width, ~300 km in length and ~60 m in depth (Gao et al., 2018), and likely controlled the formation and spatial distribution of the Permian Mn ore-rich deposits in South China. A suite of notable cherts also developed along the bottom of the Mn ore beds in the platform gullies. These formations clearly differ from the light-colored carbonates of the shallow-water platform sedimentary facies that are present on either side of the gullies. A layer of flood basalt overlies the Gexue and Nayong Mn deposits in the intermediate zone of the ELIP, while the Zunyi Mn deposit in the outer zone conformably overlies a mudstone belonging to the Longtan Formation, and its stratigraphic equivalent, the Wuchiaping Formation. Notably, there are several claystone beds at the foot and hanging walls of the ore layers in all of the Mn deposits (Fig. 2c).

The study area, Zunyi in the northern Guizhou Province, is geologically located in the outer zone of the ELIP, which contains Middle to Upper Permian sedimentary rocks including the Maokou (P_2m), Longtan (P_3l), and Changshing (P_3c) formations, but lacks strata of the Lower Permian and part of the Middle Permian (Fig. 2b). The Permian Mn deposits in Zunyi are often distributed along the limbs of a NNE-directed anticline, or in superposition to several anticlines (Fig. 2b). The Maokou Formation is composed of bioclastic limestone in the lower part and a Mn ore bearing cherty limestone in the upper part. The Longtan Formation can be subdivided into a lower argillaceous limestone and a coal-bearing upper limestone with a thickness of ~110–120 m. The overlying Changshing Formation contains >65 m of thickly bedded limestones.

A section of the Maokou Formation from an inclined shaft at the Nancha Mn ore mining district (~12 km south of the city of Zunyi) was examined here. From the base to the top, six distinct layers were identified (Fig. 2c), these include:

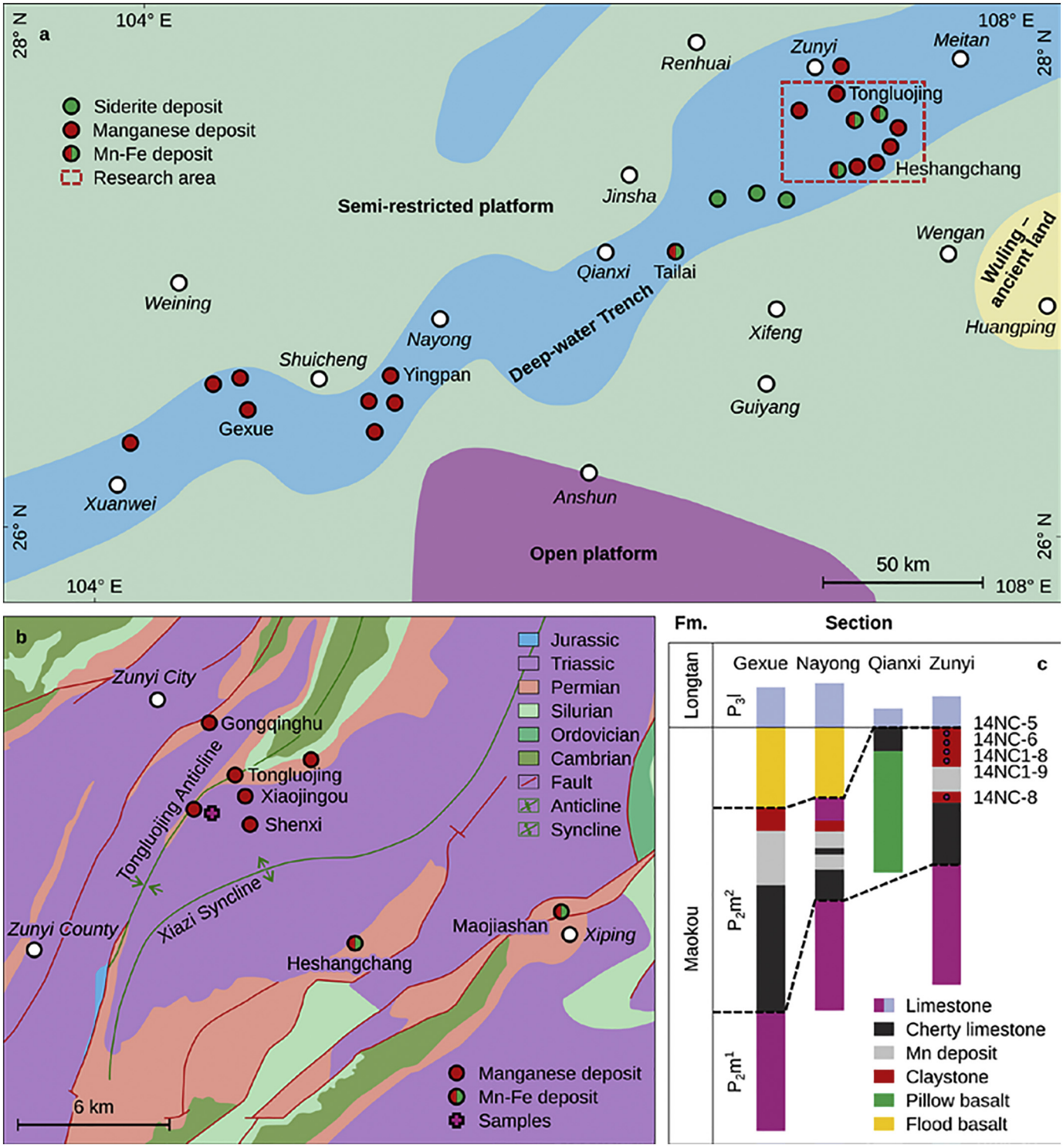

Fig. 2. (a) Map showing lithofacies distribution and palaeogeography of the late Maokou Stage of the Middle Permian in central-western Guizhou (modified from Liu et al., 2015). (b) Regional geological map of Permian sedimentary manganese deposits of the Zunyi region (modified from Gao et al., 2018). (c) Stratigraphic sections for the claystone and Mn-containing sequence of the Zunyi-Yunnan Permian manganese and claystone deposits (Gao et al., 2018), along with sample locations for this study.

Layer 1: Bioclastic limestone, the typical lower part of the Maokou Formation.

Layer 2: Cherty limestone, locally referred to as the "Bainitang Layer". Thickness is greater than 10 m.

Layer 3: Lower claystone, corresponding to the foot wall of the Mn ore. This layer is 0–0.7 m thick (averages ~0.5 m).

Layer 4: Manganese ore comprised of Mn-carbonate, clay minerals, and displaying spherulitic, oolitic, mottled, and massive structures. Thickness varies between ~0.5–2.0 m with an average of ~1.5 m.

Layer 5: Upper claystone, the hanging wall of Mn ore, containing pyrite with varied abundances. Thickness ranges from ~0–5.0 m with an average of ~2 m.

Layer 6: Argillaceous limestone, representing the lower part of the Longtan Formation. A coal bed was occasionally observed at the base; thickness exceeds 5 m.

3. Materials and methods

A total of five claystone samples were collected from the No. 2 mine (N 27°37′38.5″, E 106°55′49.3″) and No. 1 mine (N 27°37′48.4″, E 106°55′58.4″) in the Nancha Mn ore deposit. One (14NC-8) was from the lower claystone layer, and the other four (14NC-5, 14NC-6, 14NC1–8, and 14NC1–9) were from the upper claystone layer (Fig. 2c).

Major and trace elements were measured on all samples at the Testing Center of Shandong Bureau by X-ray fluorescence spectrometry (XRF) and inductively coupled plasma mass spectrometry (ICP-MS), respectively (Gao et al., 2003). The USGS rock standard GSP-1 was chosen for calibrating element concentrations of measured samples. Accuracy is estimated to within 5% for major elements and 10% for trace elements.

Zircons were extracted using standard heavy mineral separation techniques, followed by hand-picking under an optical binocular scope. Selected grains were then mounted with epoxy resin, polished to expose the center, and photographed with transmitted and reflected light as well as cathodoluminescence (CL). In-situ zircon U—Pb dating was performed using a 193 nm ArF excimer laser (RESOlution-S155) coupled to a Thermo iCAP Qc ICP-MS, with a spot diameter of 23 μm, a repetition rate of 10 Hz, and an analytical time of 40 s. Each run comprised 12 unknown sample analyses, bracketed by four zircon 91,500 standards (Wiedenbeck et al., 1995) and two Plešovice zircon standards (Sláma et al., 2008); results were treated using the ICPMSDataCal software (Liu et al., 2010). Concordia diagrams and weighted mean calculations were made using Isoplot v2.3 (Ludwing, 2003). The Plešovice zircon standard yields an average age of 338 ± 2 Ma (2σ, $n = 10$).

In-situ zircon Hf isotope analyses were made using a RESOlution-S155 193 nm ArF excimer laser, attached to a Nu Plasma II multi-collector ICP-MS, with a beam diameter of 50 μm. In order to correct for the isobaric interferences of ^{176}Lu and ^{176}Yb on ^{176}Hf, $^{176}Lu/^{175}Lu$ ratio of 0.02655 and $^{176}Yb/^{173}Yb$ ratio of 0.7965 were used (Chu et al., 2002); Hf isotope ratios were corrected to $^{179}Hf/^{177}Hf = 0.7325$ using an exponential law. Zircon Penglai was used as the reference standard, with a weighted mean $^{176}Hf/^{177}Hf$ ratio of 0.282915 ± 0.000014 (2σ, $n = 20$) during our routine analyses, similar to the reported value of 0.282906 ± 0.000010 (Li et al., 2010).

Strontium and Nd isotope analyses were made using a Finnigan Triton TI thermal ionization mass spectrometer (TIMS) at the State Key Laboratory for Mineral Deposit Research, Nanjing University, following the procedures of Pu et al. (2005). The $^{87}Sr/^{86}Sr$ and $^{143}Nd/^{144}Nd$ ratios are reported normalized to an $^{86}Sr/^{88}Sr$ ratio of 0.1194 and a $^{146}Nd/^{144}Nd$ ratio of 0.7219, respectively. Measurements of the Sr standard NIST SRM-987 yielded an $^{87}Sr/^{86}Sr$ ratio of 0.710252 ± 0.000016 (2σ, $n = 12$), and the JNdi-1 Nd standard yielded $^{143}Nd/^{144}Nd$ ratio of 0.512121 ± 0.000006 (2σ, n = 12), which is similar to the reference value of 0.512115 ± 0.000007 (Tanaka et al., 2000). Total analytical blanks were 50 pg for Sm and Nd and 0.2–0.5 ng for Rb and Sr.

For Pb isotope analyses, the samples were dissolved in Teflon vials with purified HF + HNO_3 and then separated using anion-exchange columns with diluted HBr as an eluent following the procedure described by He et al. (2005). Isotopic ratios of $^{206}Pb/^{204}Pb$, $^{207}Pb/^{204}Pb$, and $^{208}Pb/^{204}Pb$ were measured on a MC-ICP-MS at the State Key Laboratory for Mineral Deposits Research in Nanjing University. Thallium was added as an internal standard. Repeated analyses of the international Pb standard NBS981 yielded a $^{206}Pb/^{204}Pb$ ratio of 16.9327 ± 0.0005, a $^{207}Pb/^{204}Pb$ ratio of 15.4861 ± 0.0005, and a $^{208}Pb/^{204}Pb$ ratio of 36.681 ± 0.001. Using the reference values reported by Galer and Abouchami (1998) for NBS981, Pb isotopic ratios in samples were corrected for mass fractionation.

4. Results

4.1. Petrography and mineralogy

The upper claystone is gray to white and composed of clay minerals and pyrite in varied abundance (Fig. 3a). Conversely, the lower claystone is green and composed of chamosite and pyrite (Fig. 3b). Petrographic observations revealed a number of small crystal fragments of feldspar and quartz (Fig. 3c-f), and some altered volcanic shards (Fig. 3c) that are randomly distributed within the matrix. Feldspars usually display a tabular shape with or without twinning (Fig. 3d), while chamosite displays a scaly texture and occasionally retains the shape of precursor feldspar (Fig. 3e).

There are several different clay minerals. Illite and smectite (I/S) usually occur as matrix components (Fig. 4a). Kaolinite mostly occurs as discrete euhedral vermicular-shaped grains (Fig. 4a), whereas anatase occurs as subhedral polygons (Fig. 4b). Chamosite occurs as colloidal-shaped aggregates coexisting with I/S (Fig. 4c). Subhedral to euhedral polygons or short columns of the rare earth element and yttrium (REE + Y) bearing mineral bastnaesite (Fig. 4d) usually occur as disseminated grains within a berthierine matrix (Fig. 4c).

4.2. Major and trace elements

Major element concentrations are listed in Supplementary Table 1. The samples contain high SiO_2, Al_2O_3, and, in certain samples, Fe_2O_3. Loss on ignition (LOI) contents range from 8.5% to 25.2%, mostly around 13.0%. High LOI contents are consistent with a high percentage of clay minerals in these rocks. The higher Fe_2O_3 concentrations in 14NC-5 (~11.5%), 14NC1–8 (~11.6%), and 14NC-8 (~37.2%) are ascribed to the presence of pyrite and chamosite in these claystones. The wide range of MnO concentrations, from ~0.03% to ~1.9%, is attributed to the presence of Mn-carbonate minerals in some claystones. The concentration of TiO_2 is also relatively high, resulting in low Al_2O_3/TiO_2 ratios with values ranging between 2.2 and 12.6, similar to mafic volcanic rocks (~1.8–7.2, Xiao et al., 2004).

Trace element concentrations are also provided in Supplementary Table 1. Overall, the claystones are enriched in V, Cr, Co, Ni, Sc, and depleted in Th, relative to silicic tonsteins (Dai et al., 2011). Total rare earth element (REE) concentrations vary from 123 ppm to 595 ppm.

4.3. Zircon U—Pb geochronology

The U—Pb isotopic ratios of zircons are given in Supplementary Table 2. Zircons separated from the two claystone beds are mostly colorless to light yellow, although some contain dark inclusions and fractures. Zircon grains are typically euhedral with oscillatory zoning. Their lengths vary from 50 to 120 μm and widths vary from 30 to 50 μm, with length/width ratios around 3 (Fig. 5). The zircons have Th/U ratios between 0.2 and 1.1. All these features indicate the studied zircon grains are magmatic in origin.

Twenty-four zircon grains were analyzed from sample 14NC-5. The results can be divided into three age groups (Fig. 6a). Group I consists of 19 zircons with a weighted $^{206}Pb/^{238}U$ mean age of 261.6 ± 2.4 Ma (MSWD = 0.71). Group II and III yield weighted mean ages of 294.1 ± 8.3 Ma ($n = 2$, MSWD = 0.32) and 2479 ± 290 Ma ($n = 3$, MSWD = 11.6), respectively, and are likely detrital in origin.

Thirty zircon grains were obtained from sample 14NC-8 for U—Pb dating and yielded two age groups (Fig. 6b). Group I is represented by 26 zircons which gave a weighted mean $^{206}Pb/^{238}U$ age of 262.5 ± 2.3 Ma (MSWD = 1.06). Group II, comprised of the remaining 4 zircons, show more widespread ages with a weighted $^{206}Pb/^{238}U$ mean age of 313 ± 48 Ma (MSWD = 6.3).

Despite scattered zircon ages of ~270–255 Ma in Groups I of both samples (see insets in Fig. 6), these values likely represent dating uncertainty, rather than the mixing of several sediment components of

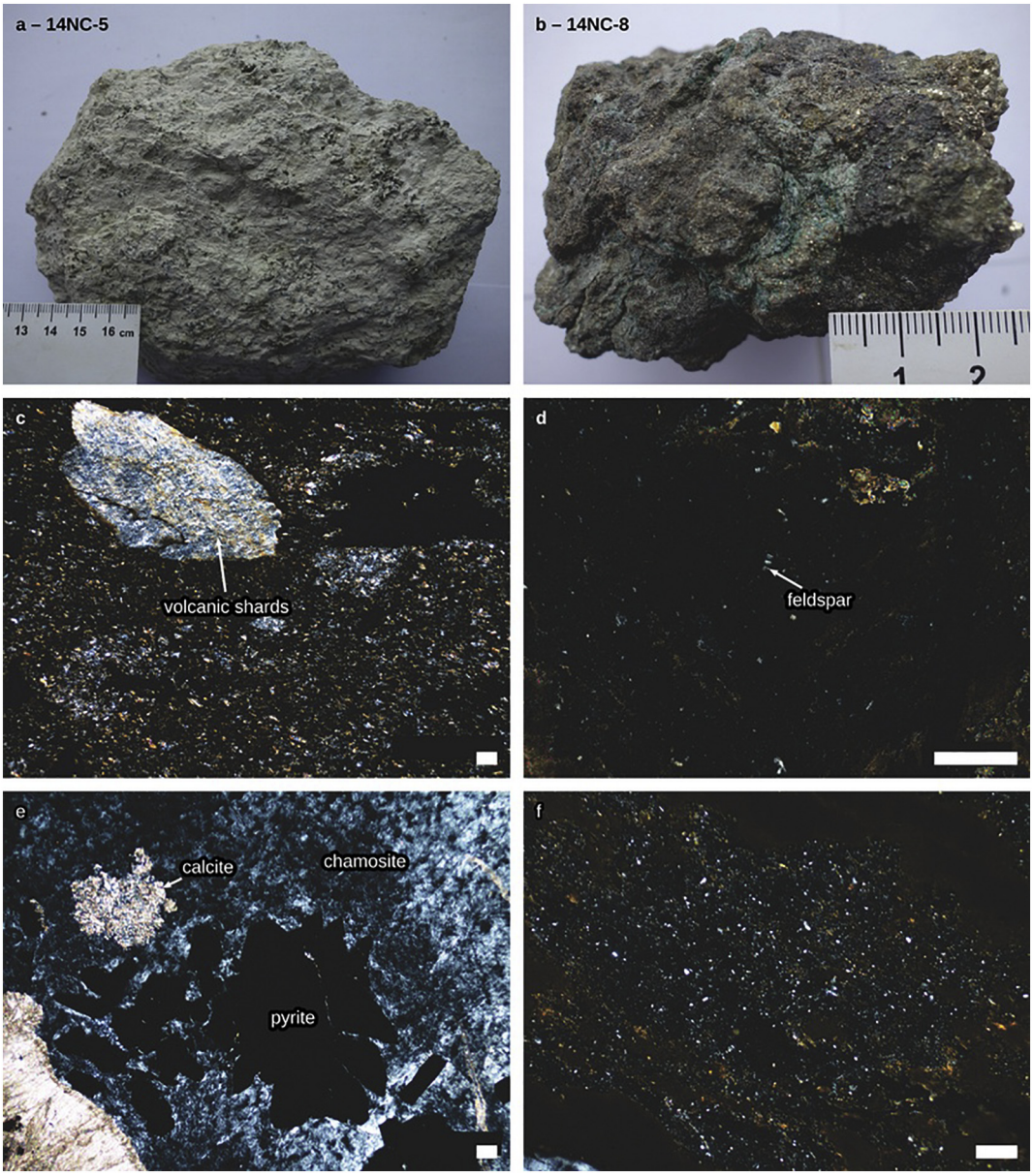

Fig. 3. Photographs and photomicrographs (cross-polarized light) of claystones from the upper Maokou Formation in the Nancha section, northern Guizhou Province, South China. (a and b) Hand specimens of the upper and lower claystones, respectively; (c) altered detritus and crystal fragments of feldspar and quartz, and volcanic shards; (d) tabular shape feldspar with multiple twins; (e) scaly chamosite and pyrite; and (f) typical tuff texture.

different ages – the <259 Ma ages are otherwise difficult to reconcile with the stratigraphic position of the claystones underneath the ~259 Ma silicic phase of ELIP magmatism (Yang et al., 2018; Zhong et al., 2014).

4.4. Zircon Hf isotopes

Hafnium isotopic compositions from samples 14NC-5 and 14NC-8 are listed in Supplementary Table 3. The Hf isotope measurements were made in the same domain as the above described U—Pb analyses (Fig. 5). A total of thirty-three analyses from sample 14NC-5 and 14NC-8 yielded relatively uniform $^{176}Hf/^{177}Hf$ ratios (0.282676 to 0.282960) and $\varepsilon_{Hf}(t)$ values between +1.7 and + 11.5, mostly concentrated between +3 to +7. One spot from sample 14NC-5 that yielded a U—Pb age of 2493 Ma gave a lower $^{176}Hf/^{177}Hf$ ratio of 0.281132 and an $\varepsilon_{Hf}(t)$ value of −0.5 (Fig. 9), further demonstrating a different origin of this zircon grain.

4.5. Sr-Nd-Pb isotopes

Isotopic compositions for Sr-Nd-Pb are provided in Supplementary Tables 4 and 5. The claystones have a narrow isotopic range for both $^{87}Sr/^{86}Sr_i$ (0.706655 to 0.706813) and $\varepsilon_{Nd}(t)$ values (−0.79 to +1.16). Similarly, initial Pb isotopic ratios fall into relatively narrow ranges, i.e., 18.349 to 18.945, for $^{206}Pb/^{204}Pb_i$, 15.583 to 15.666 for $^{207}Pb/^{204}Pb_i$, and 38.409 to 38.536 for $^{208}Pb/^{204}Pb_i$ (Fig. 8c and d).

5. Discussion

5.1. Provenance of claystones

In South China, there are a number of claystone beds associated with ELIP-volcanism; many of them are inferred to have deposited near the G-LB (259.8 ± 0.4 Ma, Henderson et al., 2012) (Fig. 1b). These can be divided into four broad types. The first type includes those related to

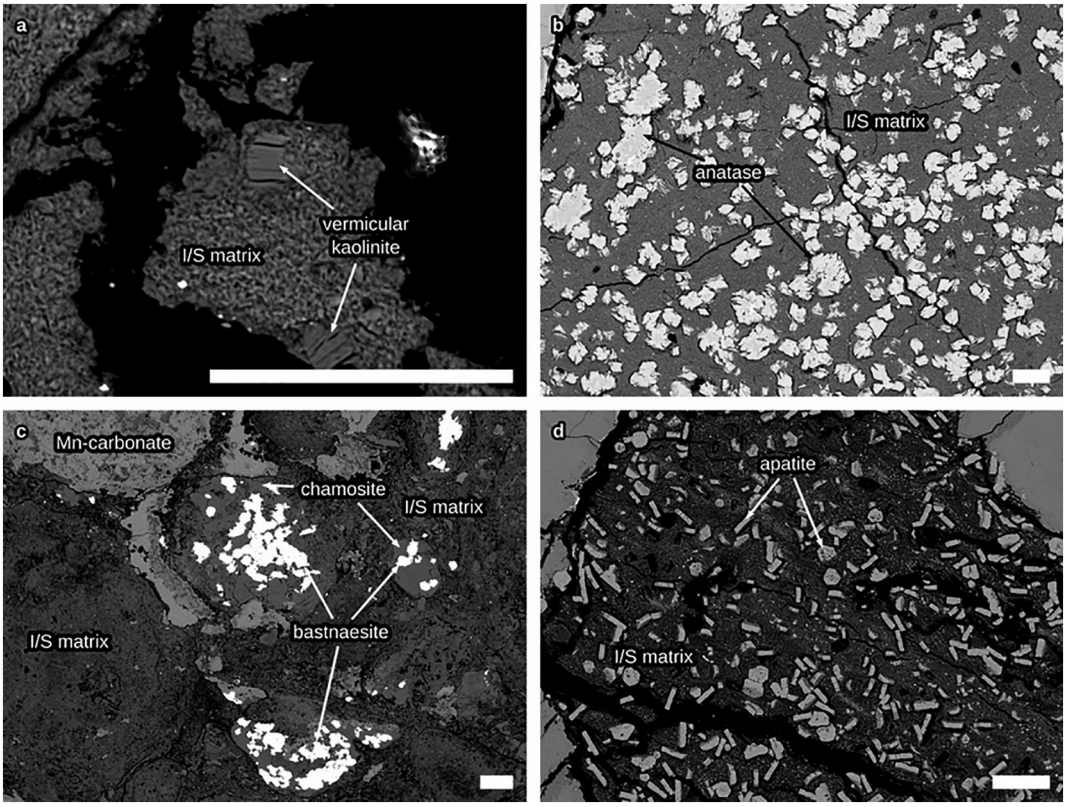

Fig. 4. Back-scattered electron images of minerals in claystones. (a) Mixed illite/smectite (I/S) matrix and vermicular kaolinite, (b) subhedral anatase, (c) chamosite altered by bastnaesite, and (d) euhedral or short columnar apatite in an I/S matrix.

the ELIP silicic volcanics. A recent study by Huang et al. (2016) analyzed the claystones of the Wangpo Bed in the Qingyin region (Fig. 1b) and suggested that they were sourced from early felsic volcanic ash. In contrast, Deconinck et al. (2014) and He et al. (2007) studied the Wangpo Bed in the Chaotian area (Fig. 1b) and argued for a possible source of terrigenous clasts from weathered silicic volcanic rocks during the later stages of the ELIP eruption. The second type includes the claystones associated with mafic ELIP volcanics, such as those in the Songzao region. Some studies suggested that they were originally mafic tuffs around the G-LB (Fig. 1b; Dai et al., 2010, 2011; Zou et al., 2016; Zhao et al., 2017). However, other studies (e.g., He et al., 2007; Huang et al., 2014; Yang et al., 2012; Liu et al., 2017) proposed that these claystone beds were generated by the weathering of the ELIP flood basalts at the top of the Maokou Formation in the Napo, Pingguo and Chaotian areas (Fig. 1b). The third type is the claystone-like bed in the Xuanwei area (Fig. 1b), which may be related to the alkaline volcanic rocks. Zhao et al. (2016) proposed that mudstone beds at the base of the Xuanwei Formation in the intermediate zone represent tuffs related to the ELIP alkaline syenitic magmatism. The fourth type of claystones from the Penglaitian section in the Laibin area (Fig. 1b) may be associated with arc-like volcanism during the evolution of the Paleo-Tethys ocean. He et al. (2014) and Zhong et al. (2013) found that these claystones were characterized by negative zircon $\varepsilon_{Hf}(t)$ values, and thus proposed that they were sourced from continental arcs. Similarly, Hou et al. (2014) and Yu et al. (2016) suggested that the claystone-like (bauxite) sediments overlying the Maokou Formation in the Leye area of the Youjiang Basin (Fig. 1b) were also likely sourced from the same arc-like volcanism, rather than the ELIP.

Based on petrographic, mineralogical, and geochemical features (see below), our claystone samples more likely originated from mafic volcanic ashes that were associated with the emplacement of the ELIP, rather than from early felsic or arc volcanic ashes, or a terrigenous clastic source of weathed flood basalts and later silicic volcanic rocks. This is evidenced by several key observations listed below.

(1) Although most of the studied samples have been intensely argillized, typical volcanic textures (Fig. 3f), shard-like morphologies (Fig. 3c), euhedral/subhedral magmatic minerals (such as apatite and anatase, Fig. 4, Jerram et al., 2016; Ukstins Peate and Bryan, 2008, Zhu et al., 2019), and vermicular kaolinite (Fig. 4a) can be identified in thin sections. Volcanic anatase has been observed to occur in altered mafic volcanic ash (Dai et al., 2014; Zhao et al., 2016). The occurrence of volcanogenic apatite in euhedral and elongate hexagonal grains is often indicative of volcanic input (Dai et al., 2017), while authigenic, vermicular-shaped kaolinite is considered to be an alteration product of volcanic glass under oxygen-poor conditions (Dai et al., 2014; Deconinck et al., 2014; Zhao et al., 2016). In summary, the petrographic and mineralogic characteristics of our samples are entirely in line with an origin from volcanic ash, as opposed to terrigenous clasts (Fig. 4).

(2) The Al_2O_3/TiO_2 ratio typically remains constant during surficial weathering, hydrothermal alteration, and volcanic processes (e.g., Dai et al., 2011; He et al., 2007) and was used here to constrain the source of material that contributed to the claystone samples (i.e. mafic, alkali, or silicic; Fig. 7d). Our samples have Al_2O_3/TiO_2 ratios of 2.2 to 12.6, consistent with values from the ELIP flood basalts (3 to 11, Xiao et al., 2004), the upper Xuanwei Formation which originated from weathered ELIP flood basalts (average 7.2, He et al., 2007), and mafic tuffs (average 8.3, Dai et al., 2011). The Al_2O_3/TiO_2 ratios are, however, distinct from values characteristic of the Wangpo claystones, the late ELIP silicic extrusive rocks, the lower Xuanwei Formation which originated from weathered ELIP silicic volcanic rocks (He et al.,

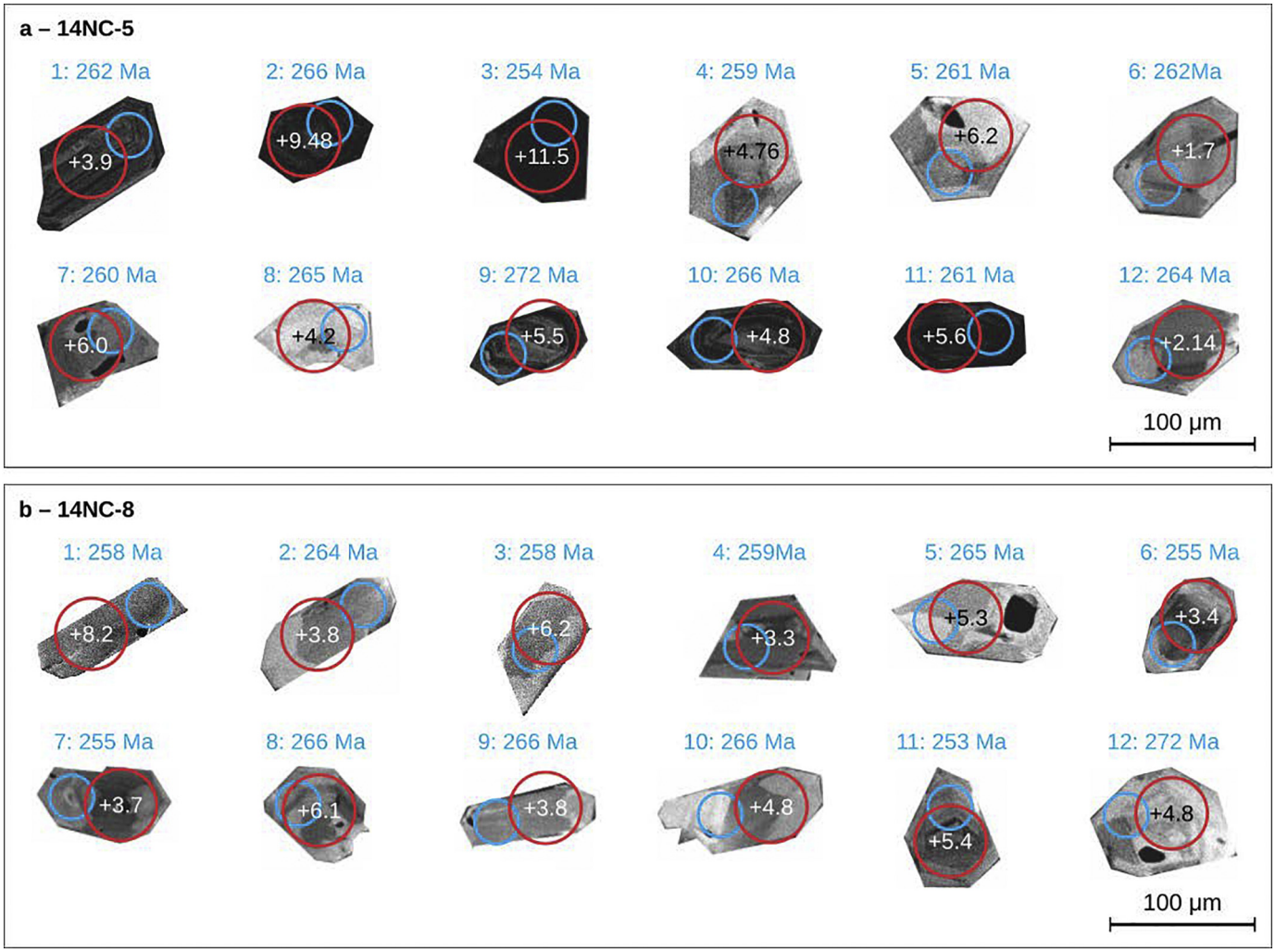

Fig. 5. Cathodoluminescence (CL) images of selected zircons from the lower (a) and upper (b) claystone layers of the upper Maokou Formation in the Nancha section, northern Guizhou Province, South China. Blue circles and numbers indicate U–Pb dates and measurement locations, red circles and numbers within indicate Hf isotope measurements ($\varepsilon_{Hf}(t)$).

2007), and silicic and alkali tonsteins (average 35, 45, 39, 60 and 23, respectively, Dai et al., 2011; He et al., 2007; Huang et al., 2016; Xu et al., 2010). Therefore the Al_2O_3/TiO_2 ratio clearly indicates a mafic source as contributing to the claystone samples reported here (Fig. 7d). Concentrations of other alteration-resistant trace elements, including V + Cr, Co + Ni, and the ratio of Th to Sc (Dai et al., 2011; Huang et al., 2016; Shellnutt and Jahn, 2010; Zhao et al., 2016), of our claystone samples are also similar to those in the Emeishan flood basalt, mafic tuffs and the upper Xuanwei Formation but distinct from those of both alkali and silicic tonsteins and silicic-related rocks in this region (Fig. 7a-c). This again supports a mafic source for the claystone samples analyzed in this study. A cross-plot of Nb/Y versus Zr/TiO_2 also consistently indicates a basaltic source (Fig. 8a).

(3) The $^{87}Sr/^{86}Sr_i$, $\varepsilon_{Nd}(t)$, and initial Pb isotopic compositions ($^{208}Pb/^{204}Pb_i$, $^{207}Pb/^{204}Pb_i$, and $^{206}Pb/^{204}Pb_i$) of all the claystone samples plot in the region of both high- and low-Ti basalts, and ultramafic intrusions (Fig. 8b-d and Fig. 9b; Liu et al., 2017; Tang et al., 2015; Zhong et al., 2011). Samples are characterized by high $^{87}Sr/^{86}Sr_i$ and low $\varepsilon_{Nd}(t)$ values, that distinguish them from the later ELIP silicic volcanic rocks which typically have low $^{87}Sr/^{86}Sr_i$ and high $\varepsilon_{Nd}(t)$ values (Fig. 8b).

(4) Another robust provenance indicator is the $\varepsilon_{Hf}(t)$ value of zircon grains (Fig. 9). As demonstrated in several previous studies (e.g., Xu et al., 2008), positive $\varepsilon_{Hf}(t)$ values are generally indicative of a mantle contribution and are considered as a common feature of intrusive ELIP mafic rock (+1.2 to +11.3; Xu et al., 2008). Zircons from the lower Xuanwei Formation have relatively high $\varepsilon_{Hf}(t)$ values (> +7; He et al., 2007), comparable with those later silicic volcanic rocks in the ELIP (~ +6 to +13; Shellnutt and Zhou, 2007; Shellnutt et al., 2009; Shellnutt and Jahn, 2010). This suggests that the late-stage silicic magmas were derived from partial melting of a mantle source without significant crustal contamination. In contrast, zircons from the Wangpo claystones have relatively low $\varepsilon_{Hf}(t)$ values of −1.8 to +3.7 (Hunag et al., 2016), which are similar to those of the ~260 Ma zircons from syenite and granitic intrusions related to the ELIP (−5.8 to +2.2; Xu et al., 2008) and clastic rocks (~30% silicic and ~70% basaltic rocks) from the late Permian Shaiwa Formation (−5.7 to +5.2; Yang et al., 2015). Such isotopic characteristics indicate a different source of more differentiated magmas involving crustal melting (Xu et al., 2008; Yang et al., 2015). Zircons with ages of ~262 Ma in our claystone samples gave $\varepsilon_{Hf}(t)$ values from −0.5 to +11.5 with the majority in the range of +2 to +7 (Fig. 9), indicating a mantle-dominated Hf composition in the zircons. This range is distinct from those of the Wangpo claystones underlying the Emeishan basalts at Qingyin and the later silicic volcanic rocks at Binchuan, but similar to those of the ELIP mafic intrusive rocks (Fig. 9). Meanwhile, $\varepsilon_{Hf}(t)$ values of our samples are completely disparate from

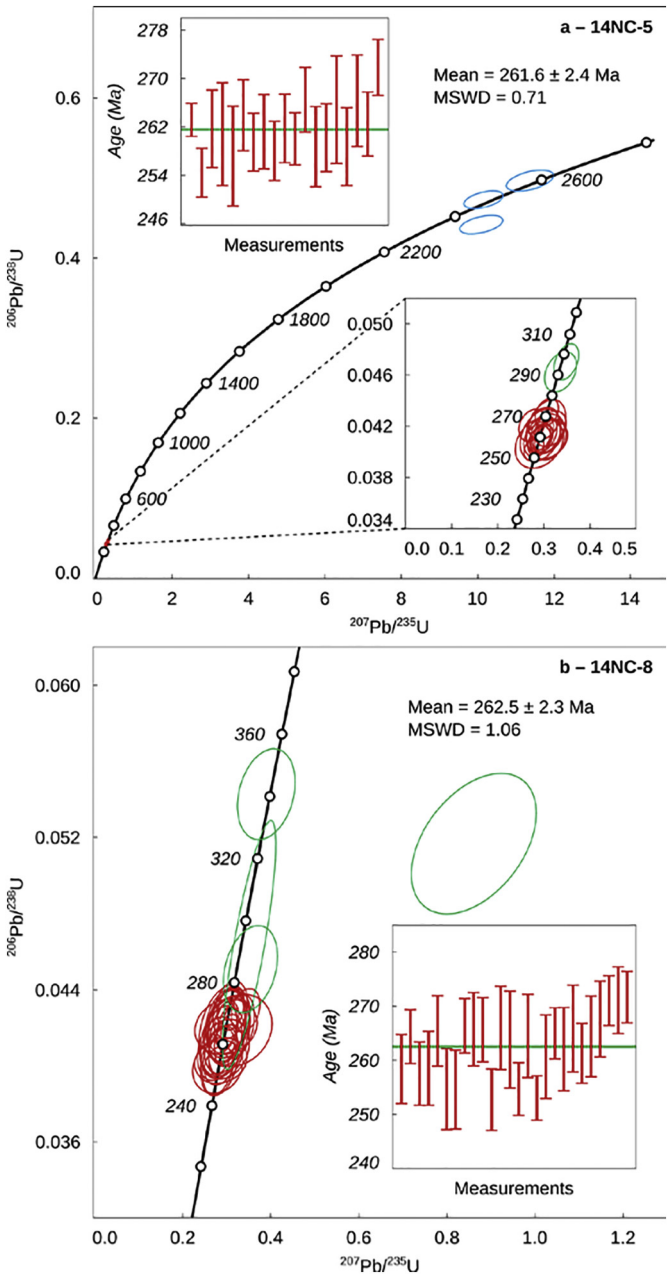

Fig. 6. Zircon U—Pb concordia diagrams of the upper (a) and the lower (b) claystone layers from the upper Maokou Formation in the Nancha section, northern Guizhou Province, South China. Different colored ellipses indicate zircon populations, as outlined in text. Insets show distribution of zircon ages around the means and a zoom-in of zircon groups I and II in panel a.

the negative zircon $\varepsilon_{Hf}(t)$ values (−9.8 to −4.3) of arc-like volcanism recorded in the regional claystones in the Laibin area, which are characteristic of continental arc sources during the contemporaneous Paleo-Tethys evolution (Zhong et al., 2013).

In light of above geochemical and stratigraphic evidence, it is likely that the claystone samples examined in this study were derived from a mafic volcanic ash related to the submarine Emeishan mafic volcaniclastics, rather than terrigenous clasts, and yet, they did not receive significant input from the ELIP felsic rocks or arc-related magmatic sources. Furthermore, the zircons in these claystones can be considered volcanic, not detrital: aside from their obtainment from these claystones with clearly volcanic textures, the zircons do not display transport-related rounding and their ages cluster tightly around ~262.5 Ma, clearly distinguished from three minor groups of detrital zircons. Therefore, these claystones can help date the elusive early mafic phase of ELIP magmatism.

5.2. Implications of the age constraints on the onset of Emeishan volcanism

Despite extensive prior work on dating the ELIP, the initiation of magmatism remains poorly constrained, making its relation to the Guadalupian mass extinction difficult to assess. The ELIP is comprised of an early-stage subaqueous mafic volcanic eruption, and subsequent subaerial flood basalts and silicic volcanism. In addition, there are also several mafic-ultramafic and felsic intrusions. Assuming that these intrusions are genetically related to the ELIP, earlier research employed micro-beam analytical techniques (i.e., SIMS and LA-ICP-MS) to constrain the timing of the ELIP magmatism to ~257–262 Ma (e.g., Guo et al., 2004; Shellnutt et al., 2012; Xu et al., 2008; Zhong et al., 2007, 2009, 2011; Zhou et al., 2002). However, in the field, the structural relationships between these intrusions and the extrusive rocks are often ambiguous.

Therefore, recent work has shifted to direct dating of extrusive rocks which has much improved the constraints on ELIP termination. Initially, a high-precision chemical abrasion TIMS (CA-ID-TIMS) age of 259.1 ± 0.5 Ma from felsic ignimbrite at the top of the flood basalt lava succession at Binchuan was put forward as the termination age of the Emeishan flood basalts (Zhong et al., 2014). This was corroborated by a nearly identical U—Pb age of 259.51 ± 0.21 Ma from the top tuff of the Puan volcanic succession (Yang et al., 2018). However, Shellnutt et al. (2020) recently pushed the ELIP termination age forward to 257.1 ± 0.6 Ma or 257.9 ± 0.3 Ma based on TIMS dating of the Tu Le rhyolite from northern Vietnam – this is the youngest volcanic unit of the ELIP, having erupted after the deposition of the Binchuan ignimbrite and the Puan tuff in South China. This younger constraint is supported by a LA-ICP-MS age of 257.8 ± 2.2 Ma (Huang et al., 2018) and a TIMS age of 257.39 ± 0.68 Ma (Zhong et al., 2020) from Upper Permian volcanic ash at Shangsi and Chaotian sections, respectively. It also fits those from the Mapojiao and Shangsi sections in the top *C. transcaucasica* zone (Bagherpour et al., 2018; Shen et al., 2011), corresponding to an absolute age of ca. 258 Ma (Ogg et al., 2016).

However, the age of ELIP initiation is still not well-constrained. The beginning of flood basalt magmatism is known to have occurred at ~260 Ma: a claystone bed directly beneath the Emeishan flood basalts, derived from early felsic tuff, yielded an age of 260.4 ± 1.2 Ma (Huang et al., 2016; Huang et al., 2018) and a similar $^{40}Ar/^{39}Ar$ age of 260.1 ± 1.2 Ma was also obtained from the Emeishan high-Ti flood basalt (Li et al., 2018). But widespread submarine pillow basalts with mafic hyaloclastite deposits that underlie the flood basalts suggest an ELIP onset age earlier than 260 Ma. For example, conodont biostratigraphy in Maokou Formation limestones, which underlie the ELIP and contain the oldest known mafic volcaniclastic debris (Sun et al., 2010), suggests a late Capitanian onset (~263 Ma; Ogg et al., 2016). Recently, Wu et al. (2020) reported CA-ID-TIMS ages of zircons from ash beds from the Capitanian series in West Texas (USA) and placed the lower Capitanian boundary age at 264.28±0.16 Ma (Wu et al., 2020).

Zircon U—Pb ages from our samples provide a crucial new constraint for the onset of the ELIP volcanism at 262.5 Ma. The stratigraphic position of the mafic claystones studied here is equivalent to those of the oldest known mafic volcaniclastic debris in the Xiongjiachang, Daqiao, Pingdi, Penglaitian, Erhai, and Dali regions (Fig. 1 and 2c). These are stratigraphically well-defined by the common deep-water cherts and cherty limestones that developed as a result of rapid subsidence prior to the onset of volcanism, consistent with the conodont biostratigraphic data of the underlying strata (~263 Ma, Ogg et al., 2016). Accordingly, the zircon ages of ~262–260 Ma may represent an early submarine stage of the Emeishan volcanism.

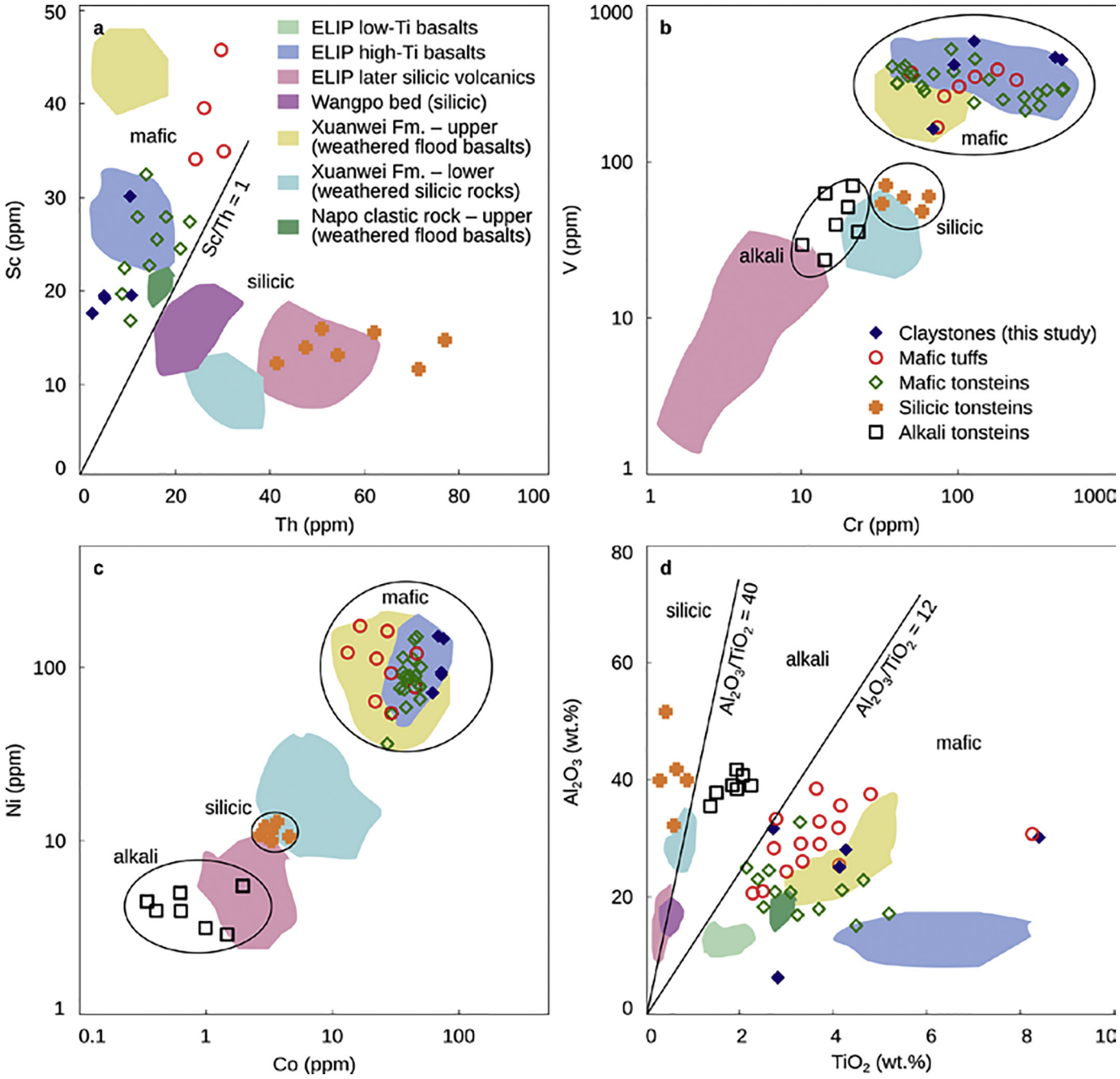

Fig. 7. Bivariate plots of (a) Sc (ppm) and Th (ppm), (b) V (ppm) and Cr (ppm), (c) Ni (ppm) and Co (ppm), and (d) TiO_2 (wt%) and Al_2O_3 (wt%) compositions of claystones from the upper Maokou Formation in the Nancha section, northern Guizhou Province, South China. Data from ELIP low-Ti basalts (Xiao et al., 2004), ELIP high-Ti basalts (Xiao et al., 2004), ELIP felsic extrusive rocks (Shellnutt and Jahn, 2010; Xu et al., 2010), the Wangpo bed (He et al., 2007; Huang et al., 2016), the upper part of the Napo clastic rocks (Huang et al., 2014), the upper Xuanwei Formation (He et al., 2007., Zhao et al., 2016), the lower Xuanwei Formation (He et al., 2007), mafic tuffs/tonsteins (Dai et al., 2011), silicic tonsteins (Dai et al., 2011), and alkali tonsteins (Dai et al., 2011) are shown for comparison.

5.3. Implications for the Guadalupian mass extinction

The Guadalupian mass extinction is one of the largest Phanerozoic extinction events (Bond et al., 2019). This event occurred in South China both within the shallow marine realm and on land (Bond et al., 2010a, 2010b; Isozaki and Aljinović, 2009). The coincident emplacement of the ELIP has previously been proposed as a trigger for the Guadalupian biotic crisis (e.g., Bond et al., 2010a; He et al., 2007, 2010; Wignall et al., 2009a, 2009b; Zhou et al., 2002).

The most notable losses during the Guadalupian mass extinction were amongst the fusulinid foraminifers (Wignall et al., 2009b; Yang et al., 2004). Based on conodont biostratigraphic data, Lai et al. (2008) and Wignall et al. (2009a) place the extinction event at the *J. xuanhanensis* conodont zone, corresponding to an absolute age of ~262 Ma (Fig. 1; Ogg et al., 2016) and the mid-Capitanian interval immediately overlain by the Emeishan LIP flood basalts. This proposed extinction event is different than the generally accepted one in the upper Capitanian and occurs before the G-LB (259.8 Ma, Henderson et al., 2012). The age of the related ELIP silicic volcanic rocks, which have been considered to be the driver of this mass extinction (He et al., 2007; Isozaki et al., 2004; Isozaki and Aljinović, 2009; Yang et al., 2015; Zhao et al., 2016), have been determined to be ~260 to 258 Ma

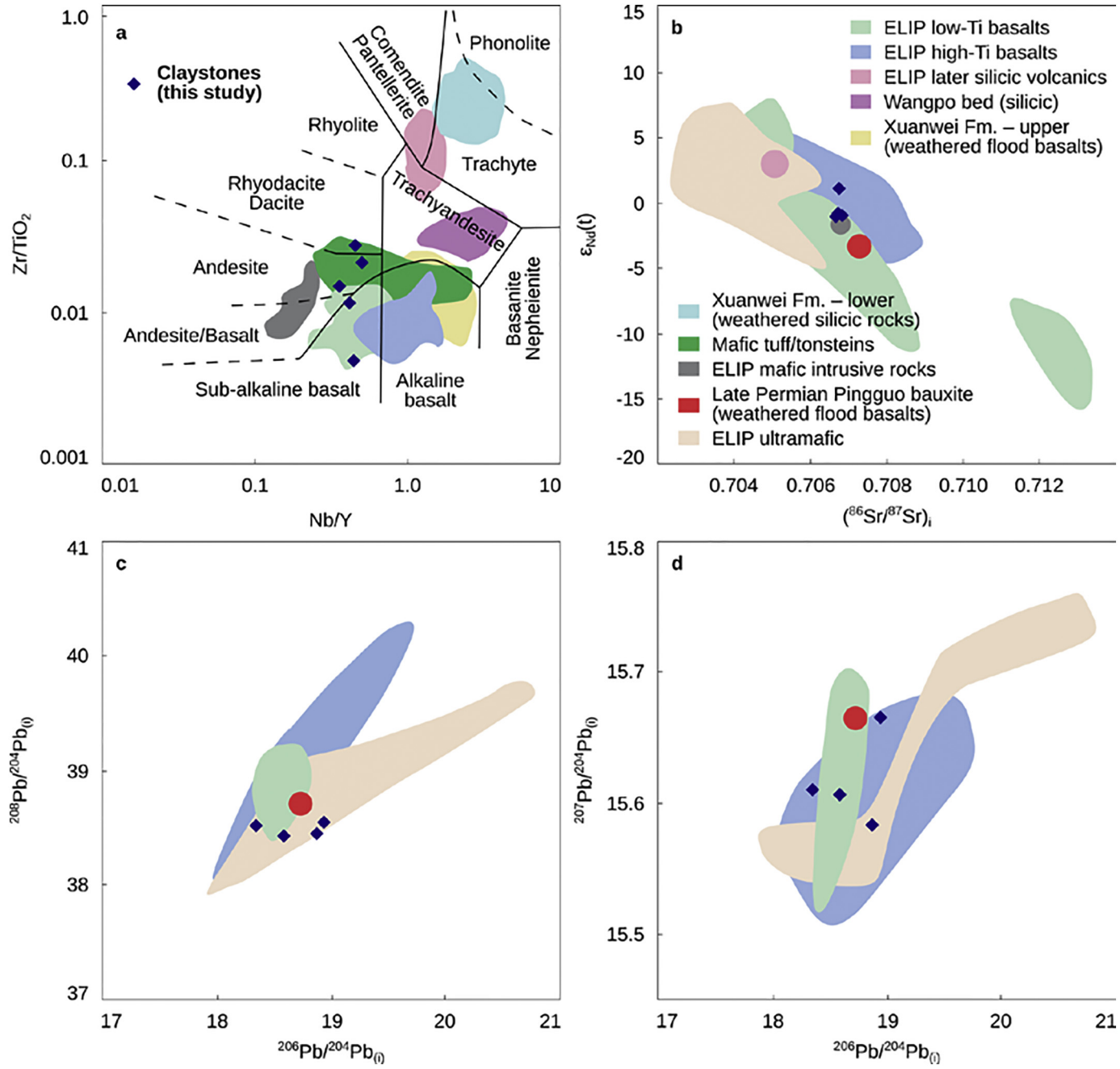

Fig. 8. Bivariate plots of (a) Zr/TiO_2 and Nb/Y, (b) $\varepsilon_{Nd}(t)$ and $(^{87}Sr/^{86}Sr)_i$, (c) $(^{208}Pb/^{204}Pb)_i$ and $(^{206}Pb/^{204}Pb)_i$, and (d) $(^{207}Pb/^{204}Pb)_i$ and $(^{206}Pb/^{204}Pb)_i$ compositions of claystones from the upper Maokou Formation in the Nancha section, northern Guizhou Province, South China. Data from ELIP low-Ti basalts (Xiao et al., 2004), ELIP high-Ti basalts (Xiao et al., 2004), ELIP mafic intrusive rocks (Tang et al., 2015), ELIP ultramafic (Liu et al., 2017), ELIP felsic extrusive rocks (Shellnutt and Jahn, 2010; Xu et al., 2010; Zhong et al., 2007), the Wangpo bed (He et al., 2007; Huang et al., 2016), the upper Xuanwei Formation (He et al., 2007), the lower Xuanwei Formation (He et al., 2007; Zhao et al., 2016), mafic tuffs/tonsteins (Dai et al., 2011), and the Late Permian Pingguo bauxite (Liu et al., 2017) are shown for comparison.

(latest Capitanian-ealiest Wuchiaping), rather than mid-Capitanian. Therefore, there is a mis-match between the previously available age constraints of the volcanism and the fusulinid extinction event, and the causes of the Guadalupian mass extinction remain cryptic.

Although the degassing of flood lava is unlikely to have more than a regional atmospheric impact (Ross et al., 2005), the occurrence of explosive mafic volcaniclastic deposits around the onset of flood volcanism has been increasingly reported from large igneous provinces (LIPs) worldwide (e.g., Jerram et al., 2009, 2016; Ross et al., 2005; Watton et al., 2013; White et al., 2009; Zhu et al., 2014, 2019). High explosive mafic volcaniclastic eruptions in submarine settings are associated with high volatile contents (CO_2, Cl, F, sulphur species), and may prove to be a previously overlooked contributor to LIP-related climate/environmental changes, such as those observed in South China.

Our data strongly supports the notion that it was the early explosive mafic stage of the ELIP that triggered the Guadalupian biotic crisis: the new 262.5 Ma age for the hydro-volcaniclastic rocks underlying the flood basalts matches with the conodont biostratigraphic data for the Guadalupian extinction event. Furthermore, the findings presented here together with the wide-spread occurrence of mafic hydro-volcaniclastic rocks throughout the ELIP (e.g., Jerram et al., 2016; Ukstins Peate and Bryan, 2008; Zhu et al., 2014, 2019) and the presence of mafic pyroclasts in the Laibin sections, 800 km east of the ELIP inner zone, paint a picture of an unusually eruptive and extremely

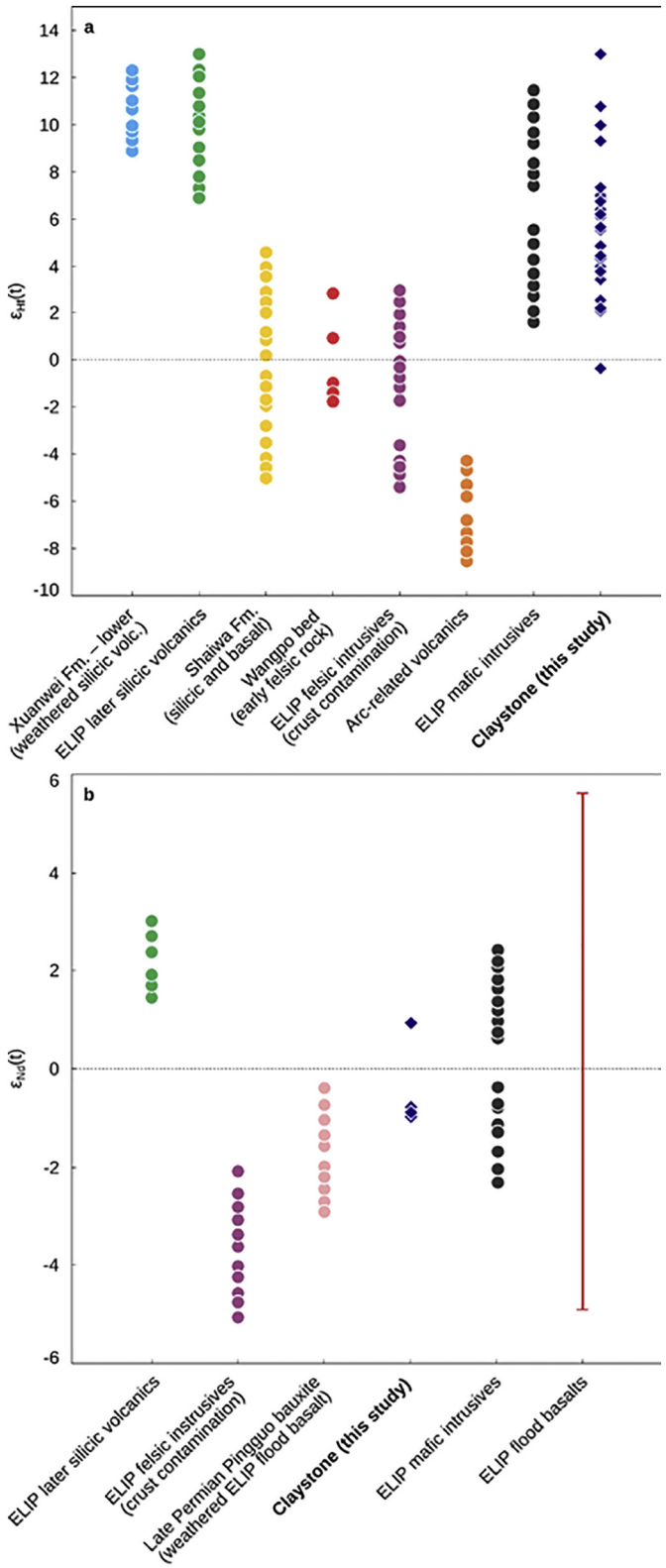

Fig. 9. Zircon $\varepsilon_{Hf}(t)$ and whole-rock $\varepsilon_{Nd}(t)$ data from claystones of the upper Maokou Formation in the Nancha section, northern Guizhou Province, South China. Data from the ELIP flood basalts (Xiao et al., 2004), ELIP mafic intrusion rocks (Tang et al., 2015; Zhong et al., 2011), ELIP felsic intrusion rocks (Xu et al., 2008), Arc-ralsted volcanic rocks (Zhong et al., 2013), ELIP felsic extrusive rocks (Shellnutt and Zhou et al., 2007; Shellnutt et al., 2009; Shellnutt and Jahn, 2010; Xu et al., 2008), Wangpo bed (Huang et al., 2016), lower Xuanwei Formation (Shellnutt et al., 2009), Shaiwa Formation (Yang et al., 2015), and Late Permian Pingguo bauxite (Liu et al., 2017) are shown for comparison.

widespread early mafic stage of Emeishan volcanism (Wignall et al., 2009a). The input of this mafic volcanic material directly into the marine environment, rather than subaerial, would have had profound consequences for marine chemistry, contributing to the environmental stresses responsible for the Guadalupian extinction event (Jerram et al., 2016). Our results further indicate that the eruption of the ELIP was a multi-phase event that was more protracted than previously thought (e.g., Huang et al., 2016; Zhong et al., 2014), and may have led to prolonged stresses on the biosphere at this time. These findings highlight the power of high-precision dating of extrusive rocks to test common assumptions about the effects of igneous processes on the major biotic events of the Phanerozoic.

6. Conclusion

Claystones at Zunyi that enclose the Mn ore beds likely lie on an isochronous horizon with the subaqueous pillow basalts and volcaniclastics in South China. Petrographic features, whole-rock geochemistry, Sr-Nd-Pb isotopic data, and zircon $\varepsilon_{Hf}(t)$ data suggest that these claystones were derived from a mafic volcanic ash related to the eruption of the Emeishan LIP. In light of the stratigraphic considerations, an age of 262.5 Ma obtained from zircons in the claystone beds is coincident with the *J. altudaensis* biostratigraphic conodont zone (~263 Ma, mid Capitanian Stage), corresponds to the eruption of early-stage Emeishan pillow basalts, and effectively represents the onset of volcanism associated with the ELIP. These new data provide important evidence for the existence of early-stage subaqueous mafic hydro-volcaniclastic ELIP volcanism and support a clear link to the Guadalupian mass extinction.

Acknowledgements

Funding for this research was provided by the National Natural Science Foundation of China (41972091), the Fundamental Research Funds for the Central Universities, China University of Geosciences in Wuhan (CUGCJ1711), and the special fund from the State Key Laboratory of Geological Processes and Mineral Resources, China University of Geosciences (no. MSFGPMR03-2). We are grateful to Dr. Kui-Dong Zhao and Wei Chen for assistance with U—Pb dating and Hf isotope analysis. We thank Dr. Sun and an anonymous reviewer for their constructive comments on earlier versions of this work and Dr. Shellnutt for editorial handling.

Declaration of Competing Interests

The authors declare that they have no known competing financial interests or personal relationships that could have appeared to influence the work reported in this paper.

Appendix A. Supplementary data

Supplementary data to this article can be found online at https://doi.org/10.1016/j.lithos.2020.105441.

References

Ali, J.R., Thompson, G.M., Zhou, M.F., Song, X., 2005. Emeishan large igneous province, SW China. Lithos 79, 475–489.

Bagherpour, B., Bucher, H., Schneebeli-Hermann, E., Vennemann, T., Chiaradia, M., Shen, S.Z., 2018. Early late Permian coupled carbon and strontiumisotope chemostratigraphy from South China: extended Emeishan volcanism? Gondwana Res. 58, 58–70.

Bond, D.P.G., Hilton, J., Wignall, P.B., Ali, J.R., Stevens, L.G., Sun, Y.D., Lai, X.L., 2010a. The Middle Permian (Capitanian) mass extinction on land and in the oceans. Earth-Sci. Rev. 109, 100–116.

Bond, D.P.G., Wignall, P.B., Wang, W., Izon, G., Jiang, H.S., Lai, X.L., Sun, Y.D., Newton, R.J., Shao, L.Y., Védrine, S., Cope, H., 2010b. The mid-Capitanian (Middle Permian) mass

extinction and carbon isotope record of South China. Palaeogeogr. Palaeoclimatol. Palaeoecol. 292, 282–294.
Bond, D.P.G., Wignall, P.B., Grasby, S.E., 2019. The Capitanian (Guadalupian, Middle Permian) mass extinction in NW Pangea (Borup Fiord, Arctic Canada): a global crisis driven by volcanism and anoxia. Geol. Soc. Am. Bull. https://doi.org/10.1130/B35281.1.
Chu, N.C., Taylor, R.N., Chavagnac, V., Nesbitt, R.W., Boella, R.M., Milton, J.A., German, C.R., Bayon, G., Burton, K., 2002. Hf isotope ratio analysis using multi-collector inductively coupled plasma mass spectrometry: an evaluation of isobaric interference corrections. J. Anal. At. Spectrom. 17, 1567–1574.
Dai, S.F., Wang, X.B., Chen, W.M., Li, D.H., Chou, C.L., Zhou, Y.P., Zhu, C.S., Li, H., Zhu, X.G., Xing, Y.W., Zhang, W.G., Zou, J.H., 2010. A high-pyrite semianthracite of Late Permian age in the Songzao Coalfield, southwestern China: Mineralogical and geochemical relations with underlying mafic tuffs. Int. J. Coal Geol. 83, 430–445.
Dai, S.F., Wang, X.B., Zhou, Y.P., Hower, J.C., Li, D.H., Chen, W.M., Zhu, X.W., Zou, J.H., 2011. Chemical and mineralogical compositions of silicic, mafic, and alkali tonsteins in the late Permian coals from the Songzao coalfield, Chongqing, Southwest China. Chem. Geol. 282, 29–44.
Dai, S.F., Li, T., Seredin, V.V., Ward, C.R., Hower, J.C., Zhou, Y.P., Zhang, M.Q., Song, X.L., Song, W.J., Zhao, C.L., 2014. Origin of minerals and elements in the late Permian coals, tonsteins, and host rocks of the Xinde Mine, Xuanwei, eastern Yunnan, China. Int. J. Coal Geol. 121, 53–78.
Dai, S.F., Ward, C.R., Graham, I.T., French, D., Hower, J.C., Zhao, L., Wang, X.B., 2017. Altered volcanic ashes in coal and coal-bearing sequences: a reviewof their nature and significance. Earth-Sci. Rev. 175, 44–74.
Deconinck, J.F., Crasquin, S., Bruneau, L., Pellenard, P., Baudin, F., Feng, Q., 2014. Diagenesis of clay minerals and K-bentonites in late Permian/early Triassic sediments of the Sichuan Basin (Chaotian section, Central China). J. Asian Earth Sci. 81, 28–37.
Editing Committee of Stratigraphy (ECS), 2000. Permian in China. Geological Publishing House, Beijing (pp149 in Chinese with English abstract).
Galer, S., Abouchami, W., 1998. Practical application of lead triple spiking for correction of instrumental mass discrimination. Mineral. Mag. 62A, 491–492.
Gao, J.B., Yang, R.D., Xu, H., Zhang, Xu., Feng, K.N., Zheng, L.L., 2018. Genesis of Permian sedimentary manganese deposits in Zunyi, Guizhou Province, SW China: Constraints from geology and elemental geochemistry. J. Geochem. Explor. 192, 142–154.
Gao, J.F., Lu, J.J., Lai, M.Y., Lin, Y.P., Pu, W., 2003. Analysis of trace elements in rock samples using HR-ICPMS. J. Nanjing University (Nat. Sci.) 39, 844–850 (in Chinese with English abstract).
Grasby, S.E., Beauchamp, B., Bond, D.P.G., Wignall, P.B., Sanei, H., 2016. Mercury anomalies associated with three extinction events (Capitanian Crisis, latest Permian Extinction and the Smithian/Spathian Extinction) in NW Pangea. Geol. Mag. 153, 285–297.
Guo, F., Fan, W.M., Wang, Y.J., Li, C.W., 2004. When did the Emeishan plume activity start? Geochronological evidence from ultramafic–mafic dikes in Southwestern China. Int. Geol. Rev. 46, 226–234.
He, B., Xu, Y.G., Chung, S.L., Xiao, L., Wang, Y., 2003. Sedimentary evidence for a rapid, kilometer-scale crustal doming prior to the eruption of the Emeishan flood basalts. Earth Planet. Sci. Lett. 213, 391–405.
He, B., Xu, Y.G., Huang, X.L., Luo, Z.Y., Shi, Y.R., Yang, Q.J., Yu, S.Y., 2007. Age and duration of the Emeishan flood volcanism, SW China: geochemistry and SHRIMP zircon U-Pb dating of silicic ignimbrites, post-volcanic Xuanwei Formation and clay tuff at the Chaotian section. Earth Planet. Sci. Lett. 255, 306–323.
He, B., Xu, Y.G., Zhong, Y.T., Guan, J.P., 2010. The Guadalupian-Lopingian boundary mudstones at Chaotian (SW China) are clastic rocks rather than acidic tuffs: implication for a temporal coincidence between the end-Guadalupian mass extinction and the Emeishan volcanism. Lithos 119, 10–19.
He, B., Zhong, Y.T., Xu, Y.G., Li, X.H., 2014. Triggers of Permo-Triassic boundary mass extinction in South China: the Siberian traps or Paleo-Tethys ignimbrite flare-up? Lithos 204, 258–267.
He, X.X., Zhu, X.K., Yang, C., Tang, S.H., 2005. High-precision analysis of Pb isotope ratios using MC-ICP-MS. Acta Geosci. Sin. 26, 19–22 (in Chinese with English abstract).
Henderson, C.M., Davydiv, V.I., Wardlaw, B.R., 2012. The Permian period. In: Gradstein, F.M., Ogg, J.G., Schmitz, M.D., Ogg, G.M. (Eds.), The Geological Timescale 2012. 2. Elsevier Press, Amsterdam, pp. 653–680.
Hou, Y.L., He, B., Zhong, Y.T., 2014. New perspective on provenance of the Permian karstic bauxite in the western Guangxi: geochemical evidence of clastic rocks of the Heshan Formation. Geotecton. Metallog. 38, 181–196 (in Chinese with English abstract).
Huang, H., Du, Y.S., Yang, J.H., Zhou, L., Hu, L.S., Huang, H.W., Huang, Z.Q., 2014. Origin of Permian basalts and clastic rocks in Napo, Southwest China: implications for the erosion and eruption of the Emeishan large igneous province. Lithos 208-209, 324–338.
Huang, H., Cawood, P.A., Hou, M.C., Yang, J.H., Ni, S.J., Du, Y.S., Yan, Z.K., Wang, J., 2016. Silicic ash beds bracket Emeishan large igneous province to <1 m.y. at ~260 Ma. Lithos 264, 17–27.
Huang, H., Cawood, P.A., Hou, M.C., Ni, S.J., Yang, J.H., Du, Y.S., Wen, H.G., 2018. Provenance of late Permian volcanic ash beds in South China: Implications for the age of Emeishan volcanism and its link age to climate cooling. Lithos 314–315, 293–306.
Isozaki, Y., Aljinović, D., 2009. End-Guadalupian extinction of the Permian gigantic bivalve Alatoconchidae: end of gigantism in tropical seas by cooling. Palaeogeogr. Palaeoclimatol. Palaeoecol. 284, 11–21.
Isozaki, Y., Yao, J.X., Matsuda, T., Sakai, H., Ji, Z.S., Shimizu, N., Kobayashi, N., Kawahata, H., Nishi, H., Takano, M., 2004. Stratigraphy of the Middle-Upper Permian and Lowermost Triassic at Chaotian, Sichuan, China Record of late Permian doublemass extinction event. Proceedings of the Japan Academy, Series B 80, 10–16.
Jerram, D.A., Single, R.T., Hobbs, R.W., Nelson, C.E., 2009. Understanding the offshore flood basalt sequence using onshore volcanic facies analogues: an example from the Faroe–Shetland basin. Geol. Mag. 146, 353–367.
Jerram, D.A., Widdowson, M., Wignall, P.B., Sun, Y.D., Lai, X.L., Bond, D.P., Torsvik, T.H., 2016. Submarine palaeoenvironments during Emeishan flood basalt volcanism, SW China: implications for plume-lithosphere interaction during the Capitanian, Middle Permian ('end Guadalupian') extinction event. Palaeogeogr. Palaeoclimatol. Palaeoecol. 441, 65–73.
Lai, X.L., Wang, W., Wignall, P.B., Bond, D., Jiang, H.S., Ali, J.R., John, E.H., Sun, Y.D., 2008. Palaeoenvironmental change during the end-Guadalupian (Permian) mass extinction in Sichuan, China. Palaeogeogr. Palaeoclimatol. Palaeoecol. 269, 78–93.
Li, X.H., Long, W.G., Li, Q.L., Liu, Y., Zheng, Y.F., Yang, Y.H., Chamberlain, K.R., Wan, D.F., Guo, C.H., Wang, X.C., Tao, H., 2010. Penglai zircon megacrysts: a potential new working reference material for microbeam determination of Hf-O isotopes and U-Pb age. Geostand. Geoanal. Res. 34, 117–134.
Li, Y.J., He, H.Y., Ivanov, A.V., Demonterova, E.I., Pan, Y.X., Deng, C.L., Zheng, D.W., Zhu, R.X., 2018. $^{40}Ar/^{39}Ar$ age of the onset of high-Ti phase of the Emeishan volcanism strengthens the link with the end-Guadalupian mass extinction. Int. Geol. Rev. 60 (15), 1906–1917.
Liu, X.F., Wang, Q.F., Zhang, Q.Z., Yang, S.J., Liang, Y.Y., Zhang, Y., Li, Y., Guan, T., 2017. Genesis of the Permian karstic Pingguo bauxite deposit, western Guangxi, China. Mineral. Deposita 52, 1031–1048.
Liu, Y.S., Gao, S., Hu, Z.C., Gao, C.G., Wang, D.B., 2010. Continental and oceanic crust recycling-induced melt-peridotite interactions in the Trans-North China Orogen: U-Pb dating, Hf isotopes and trace elements in zircons from mantle xenoliths. J. Petrol. 51 (1–2), 537–571.
Liu, Z.C., Wang, C., Zhang, Y.G., Fang, B., Chen, D., Wei, Z.Q., Cui, Z.Q., 2015. Geochemistry and ore genesis of Zunyi Mn deposit, Guizhou Province, China. Acta Mineral. Sin. 35 (4), 481–488 (in Chinese with English abstract).
Ludwing, K.R., 2003. Isoplot. A Geochronological Toolkit for Microsoft Excel. Special Publication Berkeley Geochronology Center. pp. 1–70.
Metcalfe, I., Crowley, J.L., Nicoll, R.S., Schmitz, M., 2015. High-precision U–Pb CA-TIMS calibration of Middle Permian to lower Triassic sequences, mass extinction and extreme climate-change in eastern Australian Gondwana. Gondwana Res. 28, 61–81.
Ogg, J.G., Ogg, G., Gradstein, F.M., 2016. The Concise Geologic Time Scale 2016. Elsevier, Amsterdam, pp. 123–124.
Pu, W., Gao, J.F., Zhao, K.D., Ling, H.F., Jiang, S.Y., 2005. Separation method of Rb-Sr, Sm-Nd using DCTA and HIBA. J. Nanjing University (Nat. Sci.) 41, 445–450 (in Chinese with English abstract).
Ross, P.S., Ukstins Peate, I.S., McClintock, M.K., et al., 2005. Mafic volcaniclastic deposits in flood basalt provinces: a review. J. Volcanol. Geotherm. Res. 145, 281–314.
Saitoh, M., Isozaki, Y., Yao, J.X., Ji, Z.S., Ueno, Y., Yoshida, N., 2013. The appearance of an oxygen-depleted condition on the Capitanian disphotic slope/basin in South China: Middle-Upper Permian stratigraphy at Chaotian in northern Sichuan. Glob. Planet. Chang. 105, 180–192.
Shao, T.Q., Tang, H.H., Liu, Y.H., Jiang, K.T., Hu, B., Jia, C.H., Wang, Q., Zhang, Y.N., Zhang, H., Qin, J.C., 2017. Genetic analysis of bentonite-Permian Wangpo shale in Liangshan, Hanzhong, South Shaanxi Province. Geol. J. 52, 132–141.
Shellnutt, J.G., 2014. The Emeishan large igneous province: a synthesis. Geosci. Front. 5, 369–394.
Shellnutt, J.G., Jahn, B.M., 2010. Formation of the late Permian Panzhihua plutonic-hypabyssal-volcanic igneous complex: implication for the genesis of Fe-Ti oxide deposits and A-type granites of SW China. Earth Planet. Sci. Lett. 289, 509–519.
Shellnutt, J.G., Zhou, M.F., 2007. Permian peralkaline, peraluminous and metaluminous A-type granites in the Panxi district, SW China: their relationship to the Emeishan mantle plume. Chem. Geol. 243, 286–313.
Shellnutt, J.G., Wang, C.Y., Zhou, M.F., Yang, Y.H., 2009. Zircon Lu-Hf isotopic compositions of metaluminous and peralkaline A-type granitic plutons of the Emeishan large igneous province (SW China): constraints on the mantle source. J. Asian Earth Sci. 35, 45–55.
Shellnutt, J.G., Denyszyn, S.W., Mundil, R., 2012. Precise age determination of mafic and felsic intrusive rocks from the Permian Emeishan large igneous province (SW China). Gondwana Res. 22, 118–126.
Shellnutt, J.G., Pham, T.T., Denyszyn, S.W., Yeh, M.W., Tran, T.A., 2020. Magmatic duration of the Emeishan large igneous province: insight from northern Vietnam. Geology https://doi.org/10.1130/G47076.1.
Shen, S.Z., Crowley, J.L., Wang, Y., Bowring, S.A., Erwin, D.H., Sadler, P.M., Cao, C.Q., Rothman, D.H., Henderson, C.M., Ramezani, J., 2011. Calibrating the end-Permian mass extinction. Science 334, 1367–1372.
Sláma, J., Košler, J., Condon, D.J., Crowley, J.L., Gerdes, A., Hanchar, J.M., Horstwood, M.S.A., Morris, G.A., Nasdala, L., Norberg, N., Schaltegger, U., Schoene, B., Tubrett, M.N., Whitehouse, M.J., 2008. Plešovice zircon - a new natural reference material for U-Pb and Hf isotopic microanalysis. Chem. Geol. 249, 1–35.
Sun, Y.D., Lai, X.L., Jiang, H.S., Luo, G.M., Sun, S., Yan, C.B., Wignall, P.B., 2008. Guadalupian (Middle Permian) conodont faunas at Shangsi Section, Northeast Sichuan Province. J. China Univ. Geosci. 19, 451–460.
Sun, Y.D., Lai, X.L., Wignall, P.B., Widdowson, M., Ali, J.R., Jiang, H.S., Wang, W., Yan, C.B., Bond, D.P., Védrine, S., 2010. Dating the onset and nature of the middle Permian Emeishan large igneous province eruptions in SW China using conodont biostratigraphy and its bearing on mantle plume uplift models. Lithos 119, 20–33.
Tanaka, T., Togashi, S., Kamioka, H., Amakawa, H., Kagami, H., Hamamoto, T., Yuhara, M., Orihashi, Y., Yoneda, S., Shimizu, H., Kunimaru, T., Takahashi, K., Yanagi, T., Nakano, T., Fujimaki, H., Shinjo, R., Asahara, Y., Tanimizu, M., Dragusanu, C., 2000. JNdi-1: a neodymium isotopic reference in consistency with LaJolla neodymium. Chem. Geol. 168 (3–4), 279–281.
Tang, Q.Y., Li, C.S., Zhang, M.J., Lin, Y., 2015. U–Pb age and Hf isotopes of zircon from basaltic andesite and geochemical fingerprinting of the associated picrites in the Emeishan large igneous province, SW China. Mineral. Petrol. 109, 103–114.

Ukstins Peate, I., Bryan, S.E., 2008. Re-evaluating plume-induced uplift in the Emeishan large igneous province. Nat. Geosci. 1, 625–629.
Watton, T.J., Jerram, D.A., Thordarson, T., Davies, R.J., 2013. Three-dimensional lithofacies variations in hyaloclastite deposits. J. Volcanol. Geotherm. Res. 250, 19–33.
White, J.D.L., Bryan, S.E., Ross, P.S., Self, S., Thordarson, T., 2009. Physical volcanology of continental large igneous provinces: Update and review. In: Thordarson, T., Self, S., Larsen, G., Rowland, S.K., Hoskuldsson, A. (Eds.), Studies in Volcanology: The Legacy of George Walker. Special Publications of IAVCEI 2. Geological Society, London, pp. 291–321.
Wiedenbeck, M., Alle, P., Corfu, F., Griffin, W.L., Meier, M., Oberli, F., Vonquadt, A., Roddick, J.C., Speigel, W., 1995. Three natural zircon standards for U-Th-Pb, Lu-Hf, trace element and REE analyses. Geostand. Newslett. 19 (1), 1–23.
Wignall, P.B., Sun, Y.D., Bond, D.P.G., Izon, G., Newton, R.J., Védrine, S., Widdowson, M., Ali, J.R., Lai, X.L., Jiang, H.S., Cope, H., Bottrell, S.H., 2009a. Volcanism, mass extinction, and carbon isotope fluctuations in the Middle Permian of China. Science 324, 1179–1182.
Wignall, P.B., Védrine, S., Bond, D., Wang, W., Lai, X.L., Ali, J.R., Jiang, H.S., 2009b. Facies analysis and sea-level change at the Guadalupian–Lopingian Global Stratotype (Laibin, South China), and its bearing on the end-Guadalupian mass extinction. J. Geol. Soc. Lond. 166, 655–666.
Wu, Q., Ramezani, J., Zhang, H., Yuan, D.X., Erwin, D.H., Henderson, C.M., Lambert, L.L., Zhang, Y.C., Shen, S.Z., 2020. High-precision U-Pb zircon age constraints on the Guadalupian in West Texas, USA. Palaeogeogr. Palaeoclimatol. Palaeoecol. https://doi.org/10.1016/j.palaeo.2020.109668 In press.
Xiao, L., Xu, Y.G., Mei, H.J., Zheng, Y.F., He, B., Pirajno, F., 2004. Distinct mantle sources of low-Ti and high-Ti basalts from the western Emeishan large igneous province, SW China: implications for plume-lithosphere interaction. Earth Planet. Sci. Lett. 228, 525–546.
Xu, Y.G., Luo, Z.Y., Huang, X.L., He, B., Xiao, L., Xie, L.W., Shi, Y.R., 2008. Zircon U–Pb and Hf isotope constraints on crustal melting associated with the Emeishan mantle plume. Geochim. Cosmochim. Acta 72, 3084–3104.
Xu, Y.G., Chung, S.L., Shao, H., He, B., 2010. Silicic magmas from the Emeishan large igneous province, Southwest China: Petrogenesis and their link with the end-Guadalupian biological crisis. Lithos 119, 47–60.
Yang, J.H., Cawood, P.A., Du, Y.S., 2015. Voluminous silicic eruptions during late Permian Emeishan igneous province and link to climate cooling. Earth Planet. Sci. Lett. 432, 166–175.
Yang, J.H., Cawood, P.A., Du, Y.S., Condon, D.J., Yan, J.X., Liu, J.Z., Huang, Y., Yuan, D.X., 2018. Early Wuchiapingian cooling linked to Emeishan basaltic weathering? Earth Planet. Sci. Lett. 492, 102–111.
Yang, X.N., Liu, J.R., Shi, G.J., 2004. Extinction process and patterns of Middle Permian fusulinaceans in Southwest China. Lethaia 37, 139–147.
Yu, W.C., Algeo, T.J., Du, Y.S., Zhang, Q.L., Liang, Y.P., 2016. Mixed volcanogenic-lithogenic sources for the Permian bauxite deposits in southwestern Youjiang Basin, South China, and their metallogenic significance. Sediment. Geol. 341, 276–288.
Zhang, L.L., Zhang, N., Xia, W.C., 2007. Conodont succession in the Guadalupian-Lopingian boundary interval (upper Permian) of the Maoershan section, Hubei Province, China. Micropaleontology 53, 433–446.
Zhang, Z.C., Mahoney, J.J., Mao, J.W., Wang, F.H., 2006. Geochemistry of picritic and associated basalt flows of the western Emeishan flood basalt province, China. J. Petrol. 47, 1997–2019.
Zhao, L., Zhu, Q., Jia, S.H., Zou, J.H., Nechaev, V., Dai, S.F., 2017. Origin of minerals and critical metals in an argillized tuff from the Huayingshan Coalfield, southwestern China. Minerals 7 (6), 92.
Zhao, L.X., Dai, S.F., Graham, I.T., Li, X., Zhang, B.B., 2016. New insights into the lowest Xuanwei Formation in eastern Yunnan Province, SW China: implications for Emeishan large igneous province felsic tuff deposition and the cause of the end-Guadalupian mass extinction. Lithos 264, 375–391.
Zhong, H., Zhu, W.G., Chu, Z.Y., He, D.F., Song, X.Y., 2007. SHRIMP U–Pb zircon geochronology, geochemistry, and Nd–Sr isotopic study of contrasting granites in the Emeishan large igneous province, SW China. Chem. Geol. 236, 112–133.
Zhong, H., Zhu, W.G., Hu, R.Z., Xie, L.W., He, D.F., Liu, F., Chu, Z.Y., 2009. Zircon U–Pb age and Sr–Nd–Hf isotope geochemistry of the Panzhihua A-type syenitic intrusion in the Emeishan large igneous province, Southwest China and implications for growth of juvenile crust. Lithos 110, 109–128.
Zhong, H., Campbell, I.H., Zhu, W.G., Allen, C.M., Hu, R.Z., Xie, L.W., He, D.F., 2011. Timing and source constraints on the relationship between mafic and felsic intrusions in the Emeishan large igneous province. Geochim. Cosmochim. Acta 75, 1374–1395.
Zhong, Y.T., He, B., Xu, Y.G., 2013. Mineralogy and geochemistry of claystones from the Guadalupian-Lopingian boundary at Penglaitan, South China: insights into the pre-Lopingian geological events. J. Asian Earth Sci. 62, 438–462.
Zhong, Y.T., He, B., Mundil, R., Xu, Y.G., 2014. CA-TIMS zircon U-Pb dating of felsic ignimbrite from the Binchuan section: implications for the termination age of Emeishan large igneous province. Lithos 204, 14–19.
Zhong, Y.T., Mundil, R., Chen, J., Yuan, D.X., Denyszyn, S.W., Jost, A.B., Payne, J.L., He, B., Shen, S.Z., Xu, Y.G., 2020. Geochemical, biostratigraphic, and high-resolution geochronological constraints on the waning stage of Emeishan large igneous province. Geol. Soc. Am. Bull. https://doi.org/10.1130/B35464.1.
Zhou, M.F., Malpas, J., Song, X.Y., Robinson, P.T., Sun, M., Kennedy, A.K., Lesher, C.M., Keays, R.R., 2002. A temporal link between the Emeishan large igneous province (SW China) and the end-Guadalupian mass extinction. Earth Planet. Sci. Lett. 196, 113–122.
Zhou, M.F., Zhao, J.H., Qi, L., Su, W., Hu, R., 2006. Zircon U-Pb geochronology and elemental and Sr-Nd isotope geochemistry of Permian mafic rocks in the Funing area, SW China. Contrib. Mineral. Petrol. 151, 1–19.
Zhu, B., Guo, Z.J., Liu, R., Liu, D., Du, W., 2014. No pre-eruptive uplift in the Emeishan large igneous province: new evidences from its 'inner zone', Dali area, Southwest China. J. Volcanol. Geotherm. Res. 269, 57–67.
Zhu, B., Guo, Z.J., Zhang, S.N., Ukstins, I., Du, W., Liu, R.C., 2019. What triggered the early-stage eruption of the Emeishan large igneous province? Geol. Soc. Am. Bull. 131 (11), 1837–1856.
Zou, J.H., Tian, H.M., Li, T., 2016. Geochemistry and mineralogy of tuff in Zhongliangshan mine, Chongqing, southwestern China. Minerals 6 (2), 47.